

# Recovering stellar population parameters via two full-spectrum fitting algorithms in the absence of model uncertainties

Junqiang Ge,<sup>1★</sup> Renbin Yan,<sup>2</sup> Michele Cappellari,<sup>3</sup> Shude Mao,<sup>4,1,5</sup> Hongyu Li,<sup>1</sup> and Youjun Lu<sup>1</sup>

<sup>1</sup>National Astronomical Observatories, Chinese Academy of Sciences, 20 Datun Road, Beijing 100020, China

<sup>2</sup>Department of Physics and Astronomy, University of Kentucky, 505 Rose Street, Lexington, KY 40506, USA

<sup>3</sup>Sub-Department of Astrophysics, Department of Physics, University of Oxford, Denys Wilkinson Building, Keble Road, Oxford OX1 3RH, UK

<sup>4</sup>Physics Department and Tsinghua Center for Astrophysics, Tsinghua University, Beijing 100084, China

<sup>5</sup>Jodrell Bank Centre for Astrophysics, Alan Turing Building, The University of Manchester, Manchester M13 9PL, UK

Accepted 2018 May 4. Received 2018 May 3; in original form 2018 January 17

## ABSTRACT

Using mock spectra based on Vazdekis/MILES library fitted within the wavelength region 3600–7350 Å, we analyse the bias and scatter on the resulting physical parameters induced by the choice of fitting algorithms and observational uncertainties, but avoid effects of those model uncertainties. We consider two full-spectrum fitting codes: PPXF and STARLIGHT, in fitting for stellar population age, metallicity, mass-to-light ratio, and dust extinction. With PPXF, we find that both the bias  $\mu$  in the population parameters and the scatter  $\sigma$  in the recovered logarithmic values follows the expected trend  $\mu \propto \sigma \propto 1/(S/N)$ . The bias increases for younger ages and systematically makes recovered ages older,  $M_*/L_r$  larger and metallicities lower than the true values. For reference, at  $S/N = 30$ , and for the worst case ( $t = 10^8$  yr), the bias is 0.06 dex in  $M_*/L_r$ , 0.03 dex in both age and  $[M/H]$ . There is no significant dependence on either  $E(B - V)$  or the shape of the error spectrum. Moreover, the results are consistent for both our 1-SSP (simple stellar population) and 2-SSP tests. With the STARLIGHT algorithm, we find trends similar to PPXF, when the input  $E(B - V) < 0.2$  mag. However, with larger input  $E(B - V)$ , the biases of the output parameter do not converge to zero even at the highest  $S/N$  and are strongly affected by the shape of the error spectra. This effect is particularly dramatic for youngest age ( $t = 10^8$  yr), for which all population parameters can be strongly different from the input values, with significantly underestimated dust extinction and  $[M/H]$ , and larger ages and  $M_*/L_r$ . Results degrade when moving from our 1-SSP to the 2-SSP tests. The STARLIGHT convergence to the true values can be improved by increasing Markov Chains and annealing loops to the ‘slow mode’. For the same input spectrum, PPXF is about two order of magnitudes faster than STARLIGHT’s ‘default mode’ and about three order of magnitude faster than STARLIGHT’s ‘slow mode’.

**Key words:** galaxies: evolution – galaxies: fundamental parameters – galaxies: stellar content.

## 1 INTRODUCTION

One important way of understanding galaxy formation and evolution is to constrain stellar population properties with stellar population synthesis. However, due to the degeneracy of different parameters, such as age, metallicity, dust extinction, and initial mass function (IMF), and due to uncertainties in stellar evolution model and stellar spectral library, results from stellar population synthesis

may vary with different algorithms and stellar population models (see reviews in Walcher et al. 2011; Conroy 2013).

Stellar evolution models have been studied for many decades, initially from studying stellar populations at a certain age and metallicity (e.g. Tinsley 1968; Searle, Sargent & Bagnuolo 1973; Tinsley & Gunn 1976; Bruzual 1983), then improved to modelling stellar evolutions at the whole age and metallicity parameter spaces (Charlot & Bruzual 1991; Bruzual & Charlot 1993; Bressan, Chiosi & Fagotto 1994; Worthey 1994; Fioc & Rocca-Volmerange 1997; Maraston 1998; Leitherer et al. 1999; Vazdekis 1999; Walcher et al. 2011). With many efforts dedicated to stellar evolution theory, there

\* E-mail: jqge@nao.cas.cn

are several well-developed popular models, such as Padova (Bertelli et al. 1994; Girardi et al. 2000; Marigo et al. 2008), BaSTI (Pietrinferni et al. 2004; Cordier et al. 2007), and Geneva (Schaller et al. 1992; Meynet & Maeder 2000).

Accompanying the development of stellar evolution models, there are also two kinds of stellar population synthesis models: (1) empirical population synthesis method and (2) evolutionary population synthesis method. The first method tries to reproduce a galaxy spectrum by means of a linear combination of individual stellar spectra with various types taken from a comprehensive library (Wood 1966; McClure & van den Bergh 1968; Spinrad & Taylor 1971; Faber 1972; Bica 1988; Pelat 1998; Cid Fernandes et al. 2001; Moulataka et al. 2004). The second method was developed at almost the same time by comparing galaxy data with synthesized stellar population spectrum based on stellar evolution theory, and with the IMF, star formation and chemical histories as main adjustable parameters (Tinsley 1978; Bruzual 1983; Arimoto & Yoshii 1987; Guiderdoni & Rocca-Volmerange 1987; Buzzoni 1989; Bruzual & Charlot 1993; Bressan, Chiosi & Fagotto 1994; Worthey 1994; Leitherer & Heckman 1995; Fioc & Rocca-Volmerange 1997; Maraston 1998; Vazdekis 1999; Schulz et al. 2002).

Combining with assumed IMFs and empirical stellar spectral libraries, e.g. Gunn & Stryker (1983), Pickles (1998), Jones (1999), ELODIE (Prugniel & Soubiran 2001), STELIB (Le Borgne et al. 2003), Indo-US (Valdes et al. 2004), NGSL (Gregg et al. 2006; Heap & Lindler 2011), MILES (Sanchez-Blazquez et al. 2006), IRTF (Rayner, Cushing & Vacca 2009), and the X-shooter library (Chen et al. 2011), many stellar population models are now available for full-spectrum fitting, such as BC03 (Bruzual & Charlot 2003), FSPS (Conroy, Gunn & White 2009), Vazdekis/MILES (Vazdekis et al. 2010), and M11 (Maraston & Stromback 2011).

With the improved stellar population models, faster computing capabilities, and the availability of modern spectroscopic galaxy surveys, such as the Sloan Digital Sky Survey (SDSS; York et al. 2000), the spectral population analysis has transitioned from the modelling based on a few observables, such as colours, absorption-line equivalent width, or spectral indices (e.g. Wood 1966; Faber 1972; Worthey 1994; Kauffmann et al. 2003), to the more precise pixel-by-pixel full-spectrum fitting that exploits the full spectral information (e.g. Cappellari & Emsellem 2004; Cid Fernandes et al. 2005; Tojeiro et al. 2007; Koleva 2009). The algebraic shortage, which is caused by the number of unknowns larger than observables when fitting with several colours or spectral indices, is no longer a problem in the full-spectrum fitting era. Those well-calibrated synthetic spectra at high spectral resolution have dramatically improved the possibility of using full spectrum fitting, instead of line indices, to study stellar populations. Now there are a number of spectral fitting codes, such as PPXF (Cappellari & Emsellem 2004; Cappellari 2017), STARLIGHT (Cid Fernandes et al. 2005), STECKMAP (Ocvirk et al. 2006), VESPA (Tojeiro et al. 2007), ULYSS (Koleva 2009), FIT3D (Sanchez 2011), FIREFLY (Wilkinson et al. 2015), and FADO (Gomes & Papaderos 2017), written with different algorithms.

Given all these advances of stellar population analysis methods and their wide spread applications, it is essential to understand their systematic biases and uncertainties, especially those from full-spectrum fitting methods. Only by understanding its limitations, can we truly understand its power and continue to improve it.

There have been many works focusing on the reliability test for constraining stellar population using broad-band spectral energy distributions (SED; e.g. Papovich, Dickinson & Ferguson 2001; Shapley 2001; Wuyts 2009; Muzzin et al. 2009; Lee et al. 2009). These works found that the stellar mass measurement tends to be

more reliable than others, such as stellar age, metallicity, dust extinction ( $A_V$  or  $E(B - V)$ ), and star formation rate (SFR). Considering that young stars can outshine older ones, for the one-component SED fitting, the stellar mass can be underestimated when both young and old stars exist (e.g. 19–25 per cent, Lee et al. 2009). Furthermore, the stellar mass-to-light ratios ( $M_*/L$ ) obtained from SED fitting with simple stellar population (SSP) models or single-age models are lower than those with complex star formation history (SFH) cases (Papovich, Dickinson & Ferguson 2001; Shapley 2001; Trager, Faber & Dressler 2008; Graves & Faber 2010; Pforr, Maraston & Tonini 2012). If a galaxy contains only young stars and one allows for both young and old in the fit, there will be a tendency to overestimate its mass, due to noise allowing a small amount of old models, and the biased  $M_*/L$  varies with stellar ages (Gallazzi & Bell 2009). Besides the SFH effects on the stellar population analysis, dust extinction is another important cause for bias, which can underestimate the stellar mass by 40 per cent (Zibetti, Charlot & Rix 2009).

There are already some tests based on full-spectrum fitting method, such as Cid Fernandes et al. (2005) and Ocvirk et al. (2006). Cid Fernandes et al. (2005) have checked the recovery probability of the STARLIGHT code based on mock spectra with an assumed SFH and found that the output can recover the input well but with a large scatter, which is mainly due to uncertainties introduced by error spectrum and low signal-to-noise ratio. Ocvirk et al. (2006) checked their STECKMAP code and found that two starbursts can be distinguished well only if they have an age separation larger than  $\sim 0.8$  dex with high spectral resolution ( $R = 10\,000$ ) and  $S/N (=100)$ . There is also an extinction measurement bias for different methods as shown in fig. 8 of Cid Fernandes et al. (2005). STARLIGHT tends to give lower dust extinction than the MPA/JHU data products<sup>1</sup>. In Li et al. (2017), we applied the PPXF and STARLIGHT codes for the spectral fitting of SDSS-IV/MaNGA (Bundy et al. 2015) integral field unit (IFU) data, and find that measured  $M_*/L_r$  from the two codes are consistent when  $M_*/L_r > 3$ , but a bias appears and increases with decreasing  $M_*/L_r$  when  $M_*/L_r < 3$ .

There are basically three sources that introduce the systematic biases and uncertainties in the results of a stellar population analysis. The first one is observational uncertainties such as noise in the spectra and its dependence on wavelength, and systematics in flux calibration. The second source includes inaccurate model assumptions, such as inaccuracies in the initial mass function, stellar evolution tracks, binary evolution, and stellar spectra library. Biases in model assumptions cause biases directly in the results of population analyses. The third source includes inherent degeneracies among physical parameters (e.g. age, metallicity, and extinction). Different fitting algorithms respond differently to these issues. The first and the second categories can be separately tested, but the degeneracies included in the third source are always unavoidable.

In this paper, we aim at setting a baseline for what can be recovered using spectral fitting based on the PPXF and STARLIGHT codes. Rather than studying a complex SFH, which allows a large range of possibilities and makes the results difficult to interpret, we intentionally keep the assumptions extremely simple. For simplicity, we use simulated spectra generated by one SSP and a linear combination of two SSPs to check the bias and uncertainty of the full-spectrum fitting, and only test how observational uncertainties affect the fitting results. This can tell us which kind of  $S/N$  is needed in Voronoi 2D binning (Cappellari & Copin 2003) of spectral data cubes and

<sup>1</sup><https://www.mpa.mpg.de/SDSS/>

in designing future observations. By fitting the simulated spectra with the same model assumption they are built with, we choose to ignore biases due to inaccurate model assumptions here and leave it for future investigations.

We will describe the related codes of the two full-spectrum fitting algorithms and the corresponding stellar population library in Section 2, and present the bias and scatter of different parameter estimations in Section 3. Those matters need attention when using STARLIGHT for spectral fitting and biases when applying the two codes to observations and are discussed in Section 4. Finally, we summarize our results in Section 5.

## 2 PREPARATION FOR THE TEST

In this section, we briefly introduce the related algorithms of the two spectral fitting codes, selected stellar library, and the initial parameter set-up for spectral fitting.

### 2.1 Full-spectrum fitting codes

The PPF code (Cappellari & Emsellem 2004; Cappellari 2017), which is written in both IDL and PYTHON programs (here we use the latest PYTHON version), uses a maximum penalized likelihood method in the pixel space to fit the spectra, with the line-of-sight velocity distributions (LOSVD) described by Gauss–Hermite parametrization. It uses a non-negative least-squares (NNLS) solver (Lawson & Hanson 1974) to fit for the spectral weights, embedded into a novel Levenberg–Marquardt solver adapted for bound constraints to fit the non-linear parameters, describing the galaxy kinematics and reddening. Most applications were for stellar kinematics, but there were a number of applications for stellar population analyses (Cappellari et al. 2012; Onodera et al. 2012; Morelli et al. 2013, 2015; McDermid et al. 2015; Shetty & Cappellari 2015; Li et al. 2017). The current PYTHON/IDL versions of PPF can also fit gas components at the same time.

The STARLIGHT code (Cid Fernandes et al. 2005) treats all parameters as non-linear and determines their optimal values with a simulated annealing plus Metropolis scheme to search for the minimum  $\chi^2$ . Through the Metropolis algorithm, this scheme gradually focuses on the most likely region in the parameter space by avoiding trapping in local minima. In some applications, the Markov chain generated by the Metropolis algorithm can remain trapped in a local minimum and the global convergence may not be reached (e.g. Martino, Del Olmo & Read 2012). After combining with simulated annealing to avoid trapping, Cid Fernandes et al. (2005) have checked the consistency between input versus output results, and found that the dust extinction had a clear difference with that from the MPA/JHU group. To have a thorough idea on the algorithm bias, more detailed analyses are required, which we perform in this work.

### 2.2 Stellar population library

We adopt the Vazdekis/MILES SSP library (Vazdekis et al. 2010) for full-spectrum fitting, by assuming a Salpeter IMF (Salpeter 1955) with stellar mass range  $[0.1, 100] M_\odot$ , Padova 2000 stellar evolution model (Girardi et al. 2000), and MILES stellar spectral library (Sanchez-Blazquez et al. 2006). We select a subset of 25 logarithmically spaced, equally sampled ages between 0.0631 and 15.8489 Gyr inclusive and six metallicities ( $[M/H] = -1.71, -1.31, -0.71, -0.4, 0.0, 0.22$ ).

Fig. 1 shows the parameter distributions of stellar age versus metallicity (left), and stellar age versus  $M_*/L_r$  (right). SSPs with

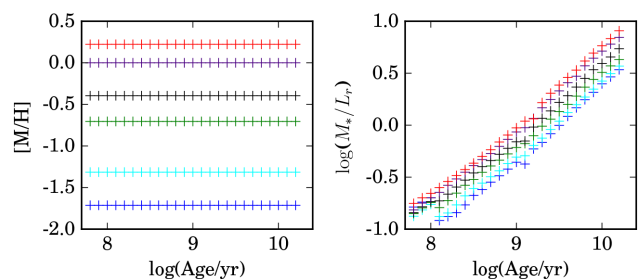


**Figure 1.** The stellar age, metallicity, and mass-to-light ratio distributions of Vazdekis/MILES stellar population library, generated by assuming a Salpeter IMF and Padova 2000 stellar evolution tracks. Left: Stellar age and metallicity distribution; Right:  $M_*/L_r$  along stellar evolution. SSPs with different metallicities are shown in different colours,  $[M/H] = -1.71$  (blue),  $-1.31$  (cyan),  $-0.71$  (green),  $-0.4$  (black),  $0.0$  (violet),  $0.22$  (red).

different metallicities are shown in different colours. The corresponding  $M_*/L_r$  are the tabulated values provided by MILES team. SSPs with the same age but higher metallicities usually have lower mass-loss rate and higher  $M_*/L_r$  (right-hand panel) than that with lower metallicities.

Since the MILES stellar spectral library has a broader fundamental parameter coverage than others (Vazdekis et al. 2010), adopting the current Vazdekis/MILES stellar population library becomes a logical choice for checking full-spectrum fitting algorithms.

### 2.3 Initial parameter set-up

We generate the mock spectra based on the Vazdekis/MILES library with  $\text{FWHM} = 2.54 \text{ \AA}$ , then use the same library for spectral fitting, to avoid biases due to incorrect model assumptions on IMFs, stellar evolution models, stellar spectral libraries, and dust extinction curves. The independent input variables include the dust extinction, age, and metallicity. The spectral fitting range of mock data is  $3600\text{--}7350 \text{ \AA}$ , which is shorter by  $\sim 50 \text{ \AA}$  than the models at both the blue and red end to make sure the model SSPs have larger spectral coverage than mock spectra.

As the SDSS-IV/MaNGA survey (Bundy et al. 2015) is planning to observe 10 000 galaxies, which has finished one half and is currently the largest galaxy sample with IFU observations, we thus set our mock spectra to mimic MaNGA’s spectral resolution with a line spread function with  $\text{FWHM} = 2.76 \text{ \AA}$  (Albareti et al. 2016). To generate a mock spectrum, we first take a template spectrum from the Vazdekis/MILES SSP library, and smooth the mock spectra from  $\text{FWHM} = 2.54\text{--}2.76 \text{ \AA}$ . All the test in our paper will feed log-rebinned spectra to the PPF and linear-rebinned spectra to STARLIGHT to fulfil the requirements of PPF and STARLIGHT codes. The velocity scale is then set to  $69 \text{ km s}^{-1}$  for spectra sampled in the logarithmic wavelength grid, and wavelength scale is set to  $1 \text{ \AA}$  for spectra sampled in the linear wavelength grid.<sup>2</sup> To make our mock spectra more like observed ones, we put in an additional velocity dispersion of  $100 \text{ km s}^{-1}$ , on top of the MaNGA spectral resolution. During the fitting, we use the full spectral information to check the algorithm precision without masking any emission-line regions. The current version of PPF code can fit both the stellar emission and gas emission together, while the STARLIGHT code can only fit

<sup>2</sup>With this sampling, the linear spectra has 3750 pixels, while the log spectrum has 3057. This implies that the effective S/N of the linear spectrum is  $\sqrt{3750/3057} \sim 11$  per cent larger.

the stellar spectra. To have a direct comparison between these two codes, we avoid tests with the emission line fitting process.

For dust extinction curves, in all the simulations, we adopt the CAL (Calzetti et al. 2000) dust extinction curve. Considering that those oldest elliptical galaxies have nearly no dust extinction, while those younger starburst galaxies or those with dust lane have higher extinction, we set the input  $E(B - V)$  from 0.0 to 0.5, which covers the typical  $E(B - V)$  ranges in the local Universe. When applying the PPF code for spectral fitting, no input parameter is modified except we limit  $E(B - V)$  fitting range to  $[-0.125, 1]$ , which corresponds to  $A_V$  range  $[-0.5, 4]$  with  $R_V = 4.05$  (Calzetti et al. 2000). The  $E(B - V)$  should be always non-negative. However, in the case of low S/N and input  $E(B - V) = 0$ , due to the large flux uncertainty, not only the spectral absorption lines but also the continuum are highly contaminated and hence can be re-shaped. Imposing strictly  $E(B - V) \geq 0$  can introduce artificially too small scatters. In order to make sure the least  $\chi^2$  is searched, negative  $E(B - V)$  is then allowed.

For the STARLIGHT code, given the range of possible configuration settings, we decided to adopt an identical configuration as used in the state-of-the-art analysis of the CALIFA (Sanchez et al. 2012) data set by de Amorim et al. (2017) and de Amorim (private communication). The STARLIGHT set-up was used to produce the CALIFA stellar population parameters publicly released in the PyCASSO data base. Specifically, we adopt the default set-up from config file ‘StCv04.C11.config’ (included in the download package<sup>3</sup>), but with the normalization window changed to that in de Amorim et al. (2017):  $\text{l\_norm} = 5635 \text{ \AA}$ ,  $\text{l\_low\_norm} = 5590 \text{ \AA}$ ,  $\text{l\_upp\_norm} = 5680 \text{ \AA}$ , and  $A_V$  fitting range to  $[-0.5, 4]$  to allow negative  $A_V$  and large enough parameter space for fitting as described in Cid Fernandes et al. (2005).

### 3 FULL-SPECTRUM FITTING TESTS

With the selected full-spectrum fitting codes and SSP library, we first test the impact of S/N and error spectra variation on the fitting results. These two tests provide guidance when analysing IFU data, on how to select S/N thresholds for Voronoi binning, and how much biases and scatters are expected given different S/N’s and error spectral shapes. These tests will be done for a single metallicity. Once we are clear about these two effects, we adopt a single set of S/N and spectral error type to test the systematic bias and scatter of the measured stellar population parameters for the whole range of metallicities.

#### 3.1 Uncertainties and systematics introduced by measurement noise

To derive the parameter bias and scatter under different spectral S/N’s, we select five SSPs with different ages ( $\log(t/\text{yr}) = 8.0, 8.5, 9.0, 9.5, 10.0$ ) but the same metallicity ( $[M/H] = 0$ ) for simulation. To generate the mock data, we assume a flat error spectrum in both linear (for STARLIGHT) and log (for PPF) binned wavelength, and seven S/N’s equally sampled in logarithmically space between 1.0 and 2.5 ( $S/N = 10, 18, 32, 56, 100, 178, 316$ ):

$$S/N = \frac{1}{N_p} \sum_i S_{\lambda i} / N_{\lambda i}, \lambda_i = [5490, 5510] \text{ \AA}. \quad (1)$$

where  $N_p$  is the number of wavelength pixels included in  $[5490, 5510] \text{ \AA}$ .

In our analysis, we mainly focus on the bias and scatter of  $E(B - V)$ ,  $M_*/L_r$ , age ( $\log t$ ), and metallicity ( $[M/H]$ ). For each mock spectrum, we perform 50 Monte Carlo simulations by assuming that the flux uncertainties at each wavelength point follow a Gaussian distribution. After the full-spectrum fitting of each simulated spectrum, we can measure the following population parameters:  $r$ -band stellar mass-to-light ratio ( $M_*/L_r$ ), luminosity-weighted age ( $t_L$ ), and metallicity ( $[M/H]_L$ ) as follows:

$$M_*/L_r = \frac{\sum f_{M,i}}{\sum f_{M,i} / (M_*/L_r)_i} \quad (2)$$

$$\log(t_L) = \sum f_{L,i} \times \log(t_i/\text{yr}), \quad (3)$$

$$[M/H]_L = \sum f_{L,i} \times [M/H]_i. \quad (4)$$

where  $(M_*/L_r)_i$ ,  $\log(t_i/\text{yr})$ , and  $[M/H]_i$  correspond to the  $r$ -band mass to light ratio, age, and metallicity of the  $i$ th SSP, while  $f_{L,i}$  and  $f_{M,i}$  are the fitted luminosity and mass fractions, respectively. We can then calculate the parameter biases for each spectrum based on 50 simulations:

$$\Delta E(B - V) = \frac{1}{N} \sum_i E(B - V)_i - E(B - V)_{\text{input}}, \quad (5)$$

$$\Delta \log(M_*/L_r) = \frac{1}{N} \sum_i \log(M_*/L_r)_i - \log(M_*/L_r)_{\text{input}}, \quad (6)$$

$$\Delta \log t_L = \frac{1}{N} \sum_i \log t_{L,i} - \log t_{\text{input}}, \quad (7)$$

$$\Delta [M/H]_L = \frac{1}{N} \sum_i [M/H]_{L,i} - [M/H]_{\text{input}}. \quad (8)$$

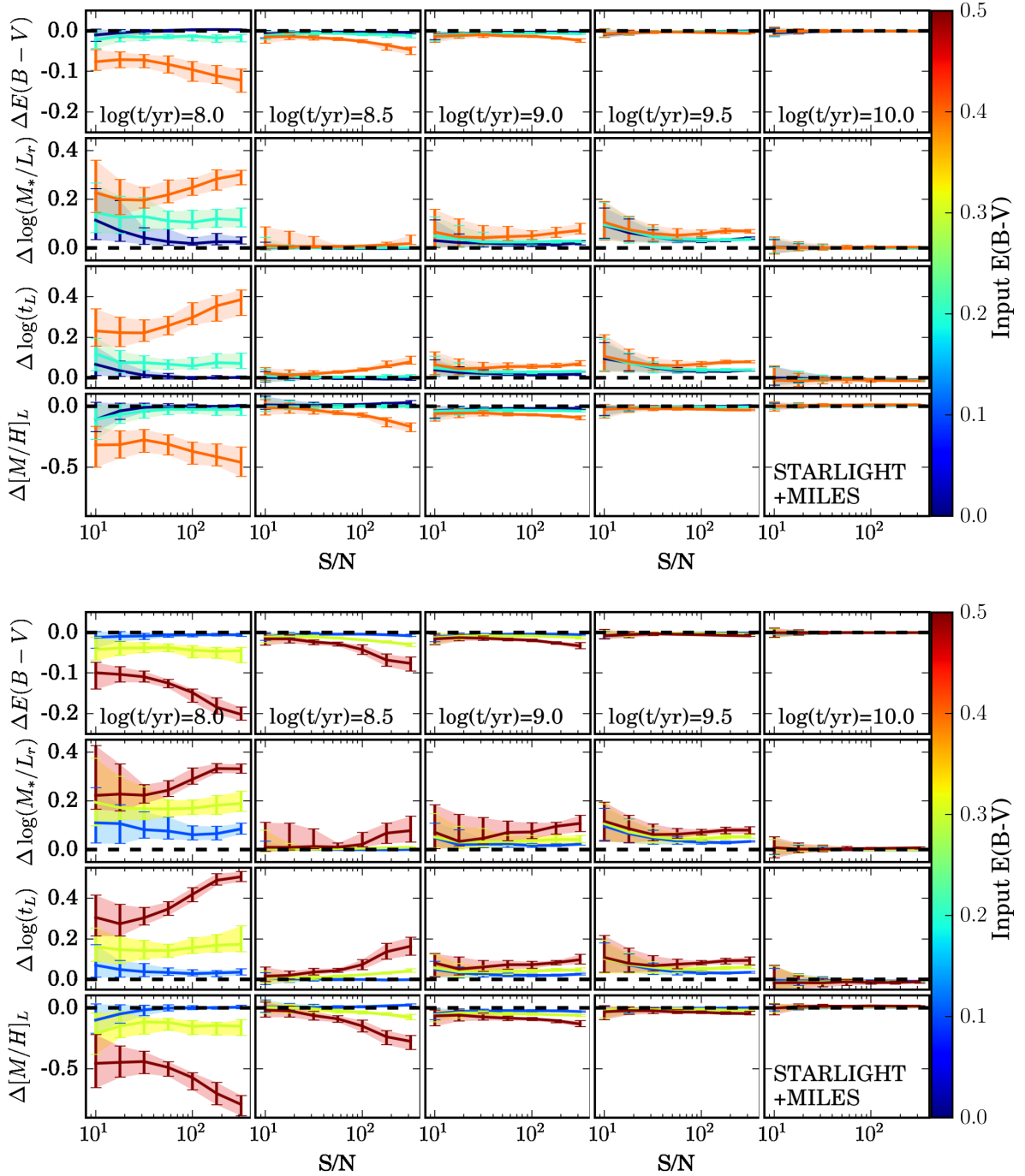
Considering that the measured parameter scatter can be non-Gaussian, we hence select the 16th and 84th percentiles of the measured parameter distribution from 50 simulations as  $1\sigma$  error bars.

Fig. 2 shows the fitting bias of measured  $E(B - V)$ ,  $M_*/L_r$ , age, and metallicity obtained from STARLIGHT fitting, population parameters are recovered well when the input  $E(B - V)$  is less than 0.2, which is consistent with the test results shown in Fig. 4 of Cid Fernandes et al. (2005), whose simulation covers the input  $A_V \leq 0.5$ . At  $E(B - V) < 0.2$ , the parameter biases and scatters decrease with increasing S/N when  $S/N < 60$ , especially for the cases of  $\Delta \log(M_*/L_r)$  (second row) and  $\Delta \log(t_L)$  (third row) at  $\log(t/\text{yr}) = 8.0$  (first column), 9.0 (third column), and 9.5 (fourth column). However, when fitting those mock spectra with input  $E(B - V) \geq 0.2$ , the bias of the four parameters does not systematically decrease with increasing S/N and  $E(B - V)$ , which is clearly shown in the  $\log(t/\text{yr}) = 8$  case: the parameter biases are roughly the same at  $S/N < 60$ , then increase when  $S/N > 60$  and input  $E(B - V) > 0.2$ . The same trends are found for the  $\log(t/\text{yr}) = 8.5, 9.0$ , and  $9.5$  cases when  $S/N > 60$ . For the old stellar population ( $\log(t/\text{yr}) = 10$ ), STARLIGHT can recover the population parameters well. There is almost no bias and the results are consistent with different input  $E(B - V)$ , and their scatters decrease with increasing S/N.

Fig. 3 shows the biases and scatters of the four parameters from the PPF fitting, which decrease uniformly with S/N and show no obvious variation for all input  $E(B - V)$  cases. For those spectra with low S/N,  $E(B - V)$  is maximally underestimated by

<sup>3</sup><http://www.starlight.ufsc.br/node/3>





**Figure 2.** The bias and scatter of four stellar population parameters obtained from STARLIGHT full-spectrum fitting by assuming different spectral S/N. The top figure represents those results with input  $E(B - V) = [0, 0.2, 0.4]$ , while the bottom one plots results with input  $E(B - V) = [0.1, 0.3, 0.5]$ . For clarity, we plot the results into two figures. For each figure, from top row to bottom row, the parameters are  $\Delta E(B - V)$ ,  $\Delta \log(M_*/L_r)$ ,  $\Delta \log(t_L/\text{yr})$ , and  $\Delta [M/H]_L$ , respectively. From left to right column, we show the results for the mock spectra with young ( $\log(t/\text{yr}) = 8.0$ ) to old stellar ages ( $\log(t/\text{yr}) = 10.0$ ), and all with solar metallicity. Lines coloured from blue to red represent the increased input  $E(B - V)$  from 0.0 to 0.5. For each line, a shaded region with a corresponding colour is added to show the parameter scatter region between the global 16th and 84th percentiles for input  $E(B - V)$  between 0 and 0.5. The horizontal dashed line at each panel shows the zero-bias positions along S/N. Each point is the median value obtained from 50 simulations. The error bars indicate the 16th and 84th percentiles.

a mean level of  $\sim 0.01$  mag. The positive biases in  $M_*/L_r$  and  $\log t_L$  are due to the fact that at low S/N one can easily hide a significant amount of mass in old populations, and the resulting redder spectrum shape can be made bluer by decreasing the

reddening. This old population will increase the  $M_*/L_r$  without contributing much to the light. The negative bias in  $[M/H]$  can be understood as due to the age-metallicity degeneracy (Worthey 1994), which states that ‘the spectrophotometric properties of an

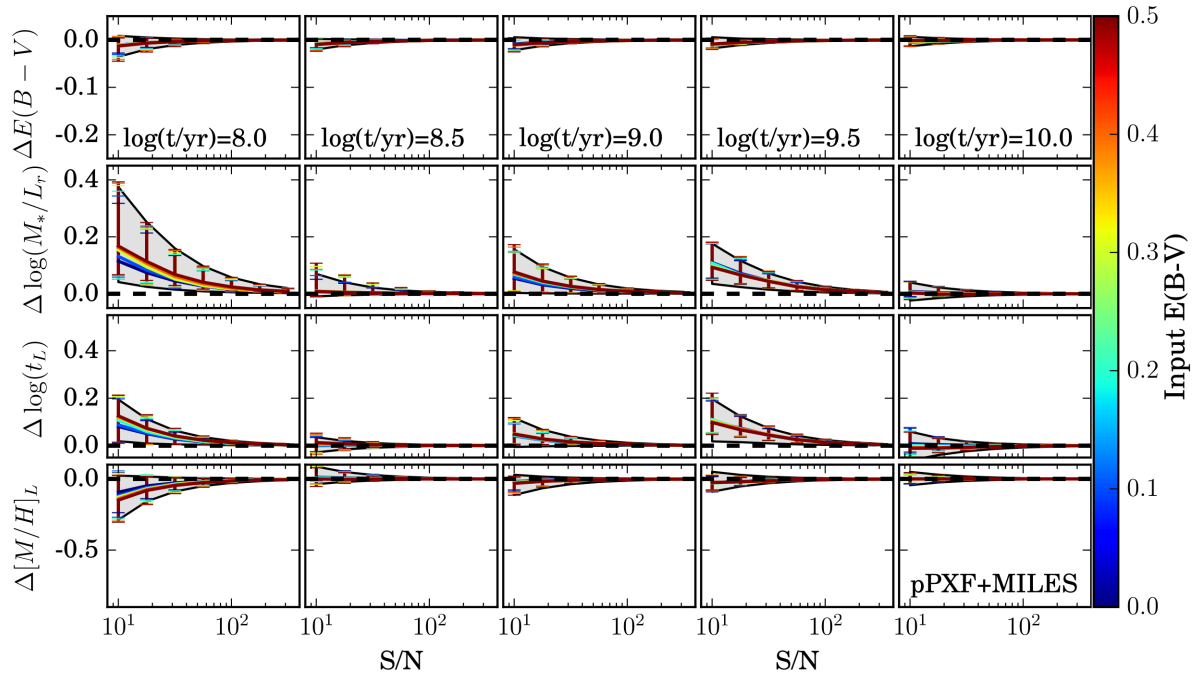


**Figure 3.** The bias and scatter of four stellar population parameters obtained from the pPXF full-spectrum fitting by assuming different spectral S/N's. Those lines, colours, and the axis coverages in each panel are the same as shown in Fig. 2. Considering that the pPXF fitting is much faster than STARLIGHT, we perform 1000 simulations for each spectrum and found that the results from input  $E(B - V) \geq 0.1$  are almost the same. Therefore, we add a grey-shaded region to each panel to show the parameter bias regions between the global 16th and 84th percentiles for input  $E(B - V)$  between 0 and 0.5.

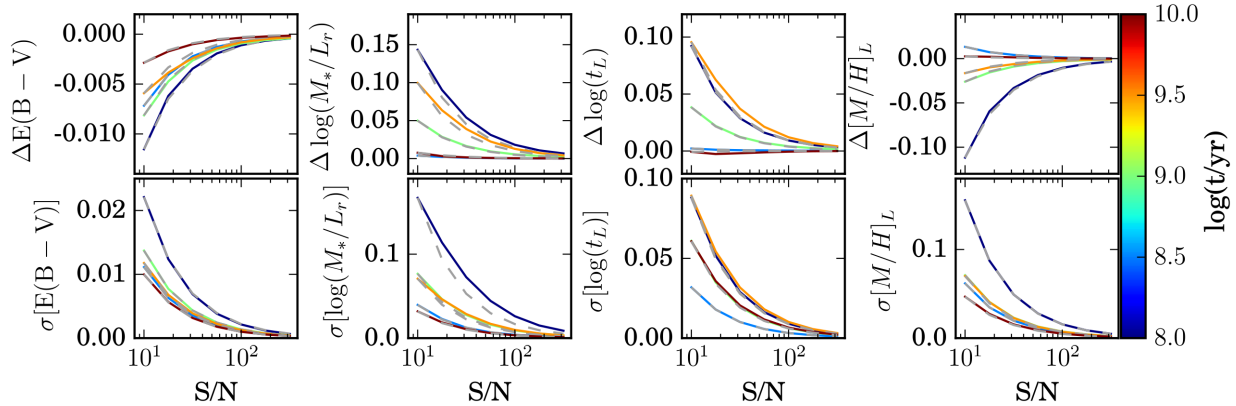


**Figure 4.** The parameter bias (top four panels) and scatter (bottom four panels) as a function of S/N for pPXF fitting based on 1000 simulations of each spectrum. The coloured lines correspond to different stellar ages. The grey dashed line in each panel shows the derived relation of  $P = k_P \times 1/(S/N)$ , where  $P$  corresponds to the parameter bias/scatter at each SSP age, and  $k_P$  shows the coefficient between  $P$  and  $1/(S/N)$  at  $S/N = 10$ . These parameter bias and scatter can be well described by  $k_P \times 1/(S/N)$  in most cases, and the corresponding coefficients are listed in Table 1. With these coefficients we can estimate the parameter bias and scatter based on  $1/(S/N)$ , which can be easily measured. Here, the parameter bias corresponds to the 50th percentile value of each parameter bias, the parameter scatter is defined as:  $\sigma(P) = \frac{1}{2}(\Delta P_{84th} - \Delta P_{16th})$ , where  $P$  corresponds to  $E(B - V)$ ,  $M_*/L_r$ ,  $\log t_L$ , and  $[M/H]_L$ ,  $\Delta P_{84th}$  and  $\Delta P_{16th}$  correspond to the parameter bias value at 84th and 16th percentiles, respectively.

unresolved stellar population cannot be distinguished from those of another population three times older and with half the metal content’.

Interestingly, although the population errors tend to be larger for younger populations, the increase is not monotonic. In fact the errors at  $\log(t/\text{yr}) = 8.5$  are actually smaller than those at  $\log(t/\text{yr}) = 9$ . This can be understood as the competition between two effects: (i) young populations have strong Balmer lines to better constrain the model fit but (ii) young populations make it more difficult to

constrain the presence of a possible old one. A sweet spot seems to be achieved between  $\log(t/\text{yr}) = 8 - 9$ .

Since the parameter bias and scatter can converge uniformly and are independent of the input  $E(B - V)$ , we then perform 1000 simulations for each spectrum in each input  $E(B - V)$  case, and calculate the global 16th and 84th percentiles of the 6000 ( $1000 \times 6$  input  $E(B - V)$ ) measured parameter biases. The grey-shaded region of each panel in Fig. 3 corresponds to the global 16th and 84th percentiles at each S/N. To get a clearer idea of how these parameter

**Table 1.**  $k_P$  at different SSP ages in the correlation:  $P = k_P \times 1/(S/N)$ .

$\log(t_{\text{SSP}}/\text{yr})$	$k_{\Delta E(B-V)}$	$k_{\Delta \log(M_*/L_r)}$	$k_{\Delta \log t_L}$	$k_{\Delta [M/H]_L}$
8.0	-0.12	1.43	0.92	-1.12
8.5	-0.07	0.04	0.02	0.13
9.0	-0.08	0.50	0.38	-0.26
9.5	-0.06	1.00	0.95	-0.16
10.0	-0.03	0.08	-0.01	0.02
	$k_{\sigma[E(B-V)]}$	$k_{\sigma[\log(M_*/L_r)]}$	$k_{\sigma(\log t_L)}$	$k_{\sigma[M/H]_L}$
8.0	0.22	1.67	0.88	1.55
8.5	0.11	0.40	0.32	0.62
9.0	0.14	0.77	0.61	0.71
9.5	0.12	0.71	0.89	0.70
10.0	0.10	0.32	0.61	0.47

biases and scatters vary with S/N, we plot the global median bias and scatter versus S/N in Fig. 4. Spectra with different ages (shown in different colours) tend to show levels of biases (top four panels) and scatters (bottom four panels). The bias and scatter are the largest for the youngest SSP and smallest for the oldest SSP. At the same time, we find that the trends of these parameter biases and scatters are described well by the expected inverse dependency on S/N:  $P = k_P \times 1/(S/N)$ , where  $P$  corresponds to the bias/scatter at different SSP ages in each panel. The grey line in each panel shows the derived parameter bias/scatter for each age based on this scaling at S/N = 10. We list all the  $k_P$  coefficients in Table 1 so that one can estimate the PPXF fitting bias/scatter for different ages.

To have a better understanding of what is causing the fitting bias, we show an example of spectral fitting details in Fig. 5. The mock spectrum is generated based on an SSP with  $\log(t/\text{yr}) = 8$ , solar metallicity, and input  $E(B - V) = 0.5$ . At high S/N ( $= 316$ ) shown in Figs 2 and 3, STARLIGHT still has parameter biases, while PPXF essentially only recovers as output the single input spectrum, as expected at this extreme S/N, with a bias and scatter less than  $\sim 0.01$  dex (Fig. 4). From the residuals we can see that PPXF yields a better fit to both the absorption-line and continuum features, but the fitting by STARLIGHT shows significant residuals for many absorption lines.

The fitting performance can be further clarified by the SFH distribution shown in the bottom two panels of Fig. 5. The PPXF solution essentially consists of a single component, the input SSP with 95 per cent of the weight, plus some minimal numerical noise. For STARLIGHT, there are significant contributions from  $\sim 1$  Gyr SSPs, which explains the large biases shown in Fig. 2.

Based on the above analysis, for PPXF fitting, the parameter biases decrease with increasing S/N. For STARLIGHT, the measured parameters converge to the input values only for cases with  $E(B - V) < 0.2$ , and show larger biases with increasing S/N for  $E(B - V) > 0.26$ . In the  $E(B - V) = 0.5$  and  $\log(t/\text{yr}) = 8$  or 8.5 cases, the increasing of parameter bias as a function of S/N starts from  $\sim S/N = 60$ . Therefore, applying S/N = 60 for further analyses tends to be a reasonable choice, those parameter biases at different S/N's can be estimated easily for both PPXF and STARLIGHT. Next, we test the dependence of the fitting results on the shape of the error spectra with spectral S/N at  $\lambda = [5490, 5510] \text{ \AA}$ .

### 3.2 Impact of error spectrum shapes

All observed spectra come with uncertainties in the flux. Full spectrum fitting codes take these uncertainties into account during fitting. This potentially leads to different spectrum regions being weighted differently in deriving the results. Could different wavelength de-

pendence in these weights lead to different biases in the fitted parameters? Here, we check the dependence of spectral fitting results on the shape of the error spectrum.

Six kinds of error spectra are designed based on the spectral types of SSPs and MaNGA error spectral types. In Fig. 6, ET1 and ET5 are consistent with the continuum slope of a young ( $10^8$  yr) and an old ( $10^{10}$  yr) SSP with solar metallicity, respectively. ET3 represents a flat error spectrum which has already been used in the S/N test above. ET2 is half way between ET1 and ET3, and is similar to the error spectra of typical MaNGA data. ET4 is half way between ET3 and ET5. ET6 is the case of a constant S/N per wavelength pixel, three spectral examples with stellar age  $\log(t/\text{yr}) = 8.0, 9.0$ , and 10.0 and solar metallicity is shown in blue, green, and red colours.

Fig. 7 shows the test results for STARLIGHT with these six types of error spectra. When the error type varies from ET1 to ET5, the measured parameter biases become smaller, especially for those spectra with high dust extinction. The ET1 error spectrum, which has the largest flux uncertainty in the blue band than the other five types, causes the largest parameter bias. The ET5 error spectrum, which has the smallest flux uncertainty in the blue band, induces the smallest parameter bias. These biases caused by error spectral shapes become smaller with increasing stellar age, and disappear at  $t = 10^{10}$  yr.

As shown in Fig. 6, many absorption features are concentrated in the blue band (e.g.  $\lambda < 5000 \text{ \AA}$ ), especially for those young SSPs (e.g. the spectrum for  $t = 10^8$  yr). Therefore, if there are higher flux uncertainties included in the blue band, the larger parameter biases and scatters are induced for STARLIGHT. The fitting biases and scatters decrease with increasing stellar ages, which correspond to increasing absorption features included in the red band.

The performance of spectral fitting with the ET6 error spectrum also verifies the above interpretation. For the  $t = 10^8$  yr case, ET1 and ET6 differ mainly at  $\lambda < 4000 \text{ \AA}$ . The flux uncertainty of ET6 at  $\lambda < 4000 \text{ \AA}$  is smaller than that of ET1, the parameter biases resulted from fitting with ET6 are smaller than those with ET1.

Compared to the STARLIGHT fitting, the PPXF fitting results show very weak or no dependence on the error spectrum types (Fig. 8) – the biases and scatters are all similar in the six cases.

After checking the effects of error spectral shapes in STARLIGHT and PPXF, we select the flat error spectrum (ET3) for studying the performance of the two codes further in the age-metallicity parameter space and two components-based SFH tests. Although ET2 is closer to observations (at least for the MaNGA survey), the error spectral shapes still have large variations for different observational instruments. Therefore, applying the flat error spectrum for fitting tests would be a reasonable choice, after which we can tell whether the fitting with an observed error spectrum will have a larger or smaller bias compared to our fiducial case.

### 3.3 Code tests with single SSP-based mock spectra

With the understanding of S/N and error spectral type effects, we can now assume a suitable S/N ( $= 60$ ) and flat error spectrum (ET3) to check the algorithm bias and scatter in the age and metallicity parameter space of the Vazdekis/MILES SSP library. Mock spectra are generated based on single SSPs with the initial set-up as described in Section 2.3. By analysing the fitting with mock spectra generated by single SSPs, we can have a thorough interpretation on (1) which kinds of spectra are easily biased, (2) when the fitting results show unavoidable biases, and (3) how large these biases and scatters are.

Fig. 9 shows the STARLIGHT fitting results in different metallicity

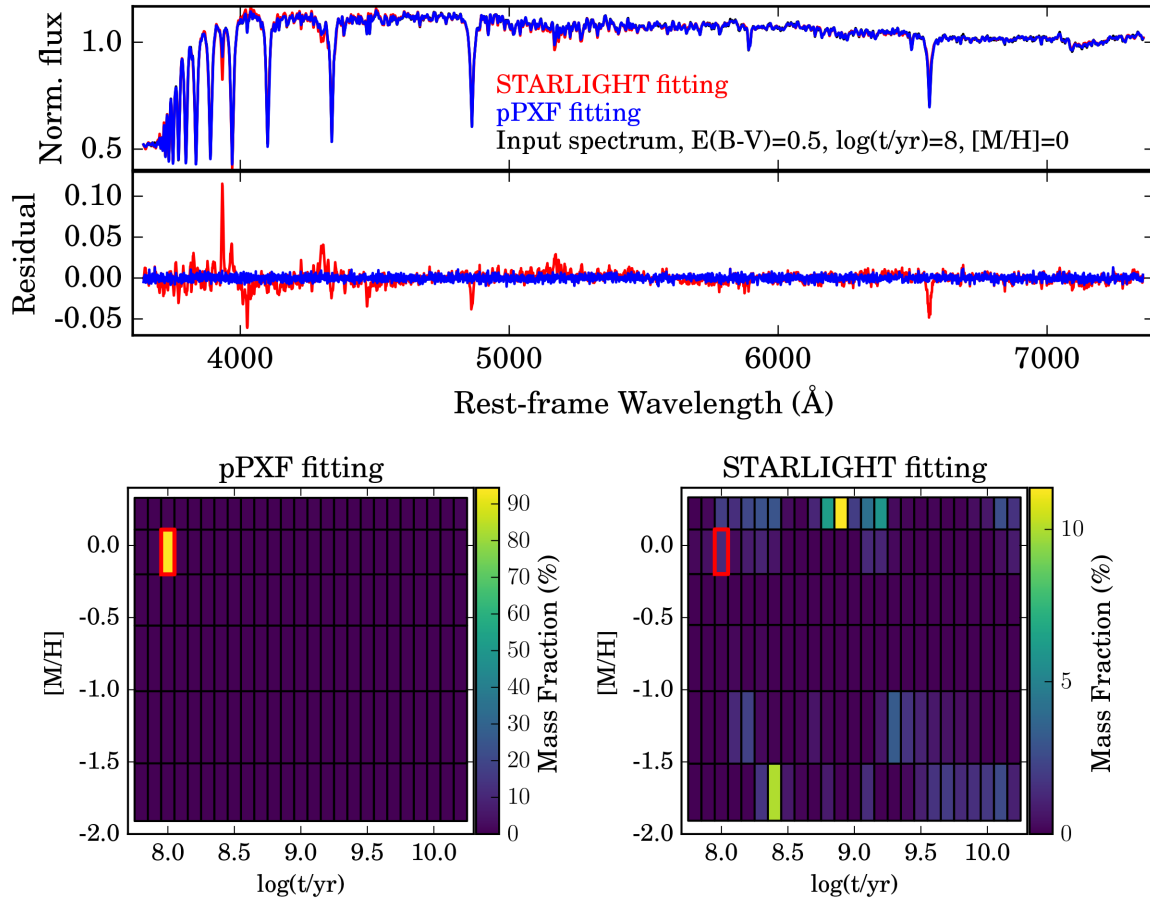


**Figure 5.** An example of the full-spectrum fitting to an SSP with solar metallicity,  $10^8$  yr age, input  $E(B - V) = 0.5$ , and  $S/N = 316$ . The fitting results and residuals by pPXF and STARLIGHT codes are shown in the top panel. The black colour shows the input spectrum, the red colour shows the fitted model spectrum, and residual by STARLIGHT, while the blue colour represents the model spectrum and residual by pPXF. The bottom left panel shows the averaged SFH map obtained from 50 Monte Carlo simulations by pPXF fitting, while the bottom right panel shows the same SFH map by STARLIGHT fitting. Each SSP is enclosed by a black box, and the colour in each black box represents the mass fraction of each SSP. The solid red box shown in each SFH map labels the position of the input SSP.

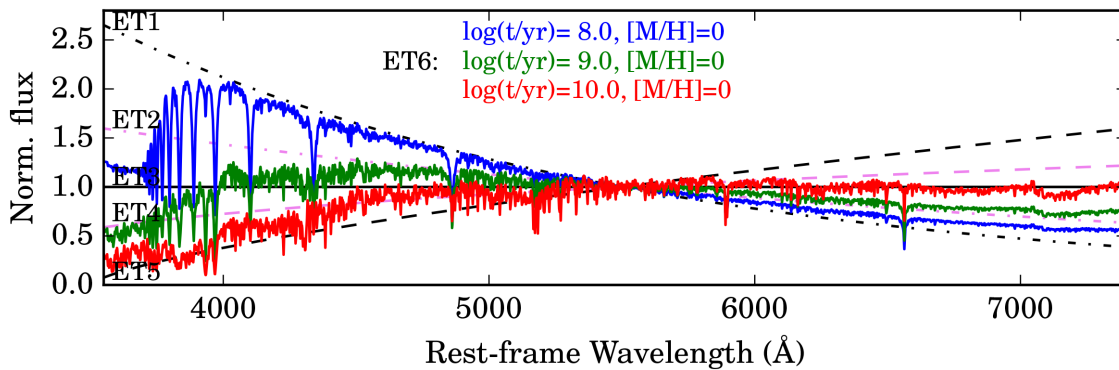


**Figure 6.** Six selected spectral error types for the flux uncertainty to test full-spectrum fitting algorithms. The five smooth curves are error type 1 (ET1) through error type 5 (ET5). ET6 is defined to have constant  $S/N$  at all wavelengths. Thus, ET6 varies with input spectrum. The three coloured error spectra show ET6 error spectra for three different SSPs with  $\log(t/\text{yr}) = 8.0, 9.0$ , and  $10.0$ , and solar metallicity.

bins with stellar ages labelled with rainbow colours. According to this plot, we summarize three typical behaviours of the STARLIGHT fitting: (1) For those SSPs with  $t < 10^9$  yr, the measured  $E(B - V)$  biases increase with increasing dust extinction for all metallicities; (2) Stellar population parameter biases increase with younger stellar

ages; and (3) For those SSPs with  $t > 10^9$  yr, the fitted population parameters show consistent results with the input values.

When fitting young SSPs with significant extinction, STARLIGHT invokes older SSPs to fit the red continuum shape, while pPXF has no problem finding the correct extinction.



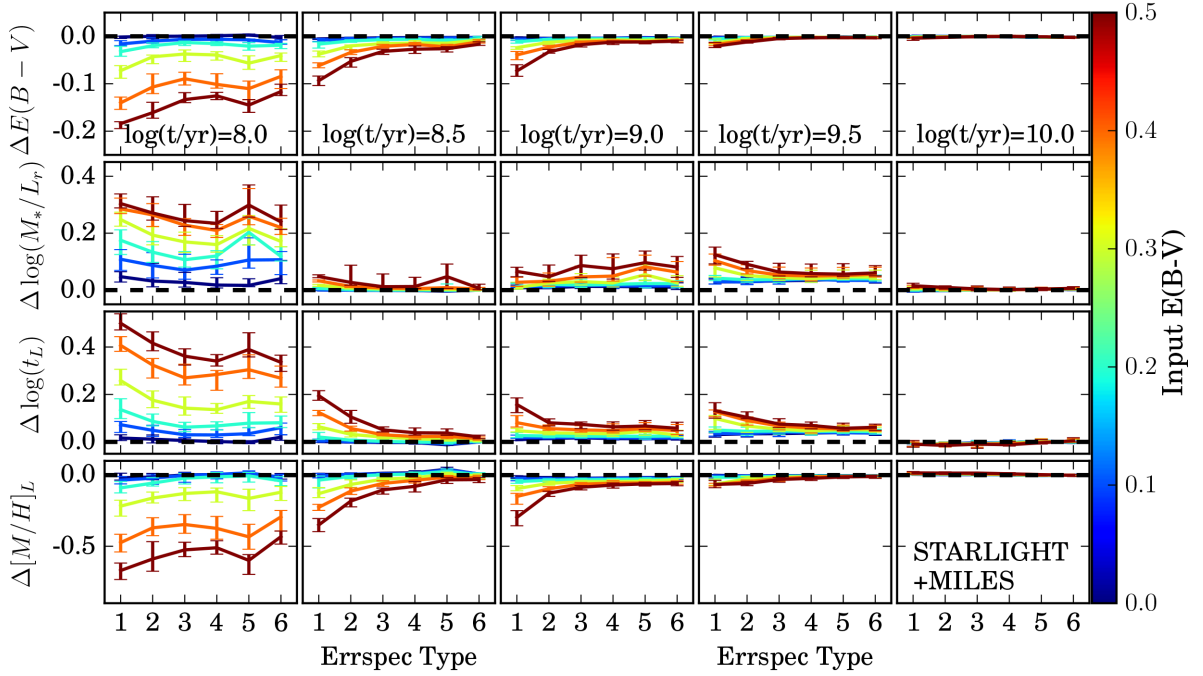


**Figure 7.** STARLIGHT fitting results at  $S/N = 60$  obtained by using different error spectral types as shown in Fig. 6. Errspec Type 1–6 represent ET1–ET6, respectively. The input  $E(B - V)$  and SSP age set-up are the same as shown in the  $S/N$  test section (Figs 2 and 3).

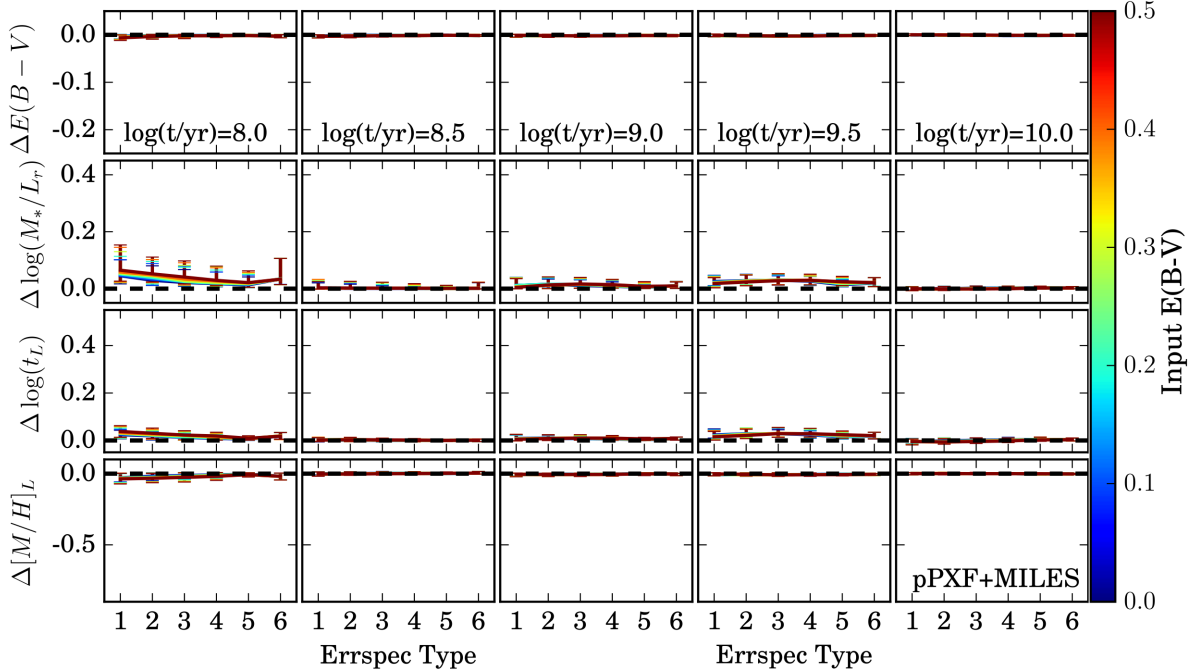


**Figure 8.** The variation of pPXF fitting results at  $S/N = 60$  with different error spectrum types, the labels, and colours are the same as shown in Fig. 7.

As shown in the top six panels of Fig. 10, the dust extinction measurements from pPXF are insensitive to the input  $E(B - V)$ , no matter what stellar metallicity is adopted. However, for each metallicity, spectra with younger ages always result in larger  $M_*/L_r$  biases, which is caused by the contamination of old populations that contributes little to the light but significantly to the mass. These artificial old SSPs have little effects on the light-weighted ages and

metallicities, but can introduce parameter scatters as shown in the third and fourth rows of Fig. 10.

### 3.4 Linear combination of two different SSPs

Considering that the SFH of a galaxy is usually not dominated by a single SSP, we test the performance of the pPXF and STARLIGHT

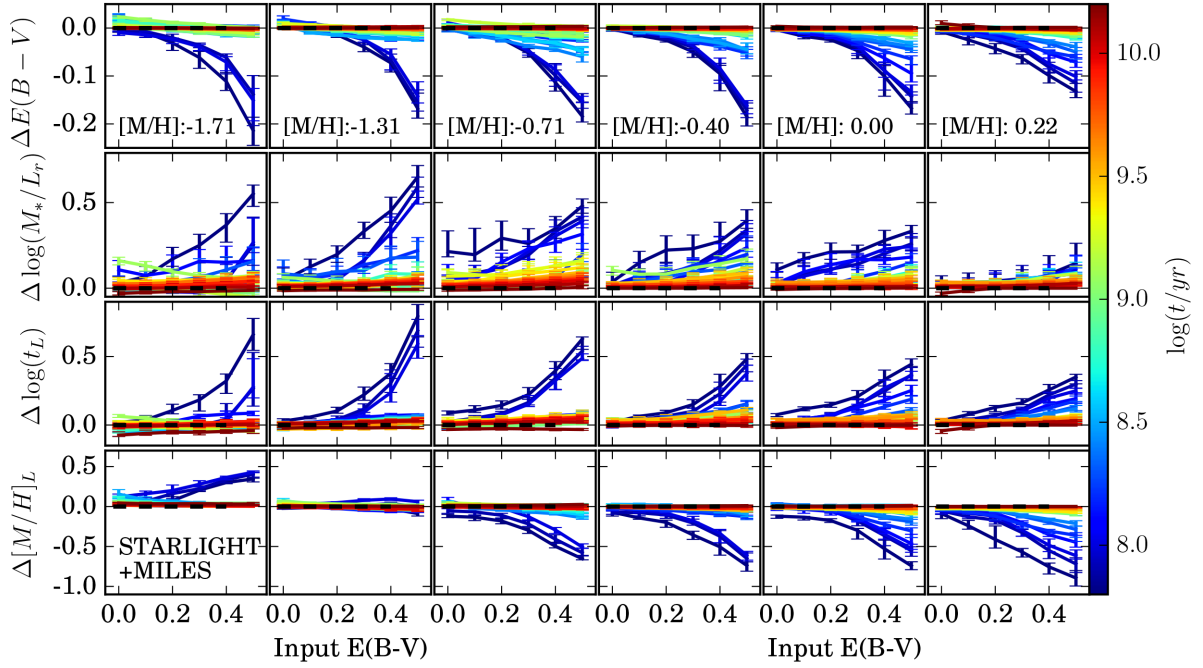


**Figure 9.** STARLIGHT fitting of mock spectra generated by a single SSP with different ages and metallicities at  $S/N = 60$ . From left to right, we show the parameter biases at different  $[M/H]$  ( $-1.71, -1.31, -0.71, -0.40, 0.00, 0.22$ ) bins. Blue to red colours represent the stellar age ranging from 0.063 to 15 Gyr. The biases in the four parameters ( $\Delta E(B-V)$ ,  $\Delta \log(M_*/L_r)$ ,  $\Delta \log(t_L)$ , and  $\Delta [M/H]_L$ ) are shown from top to bottom. The zero-biased line of each parameter in each panel is labelled as the horizontal dashed line.

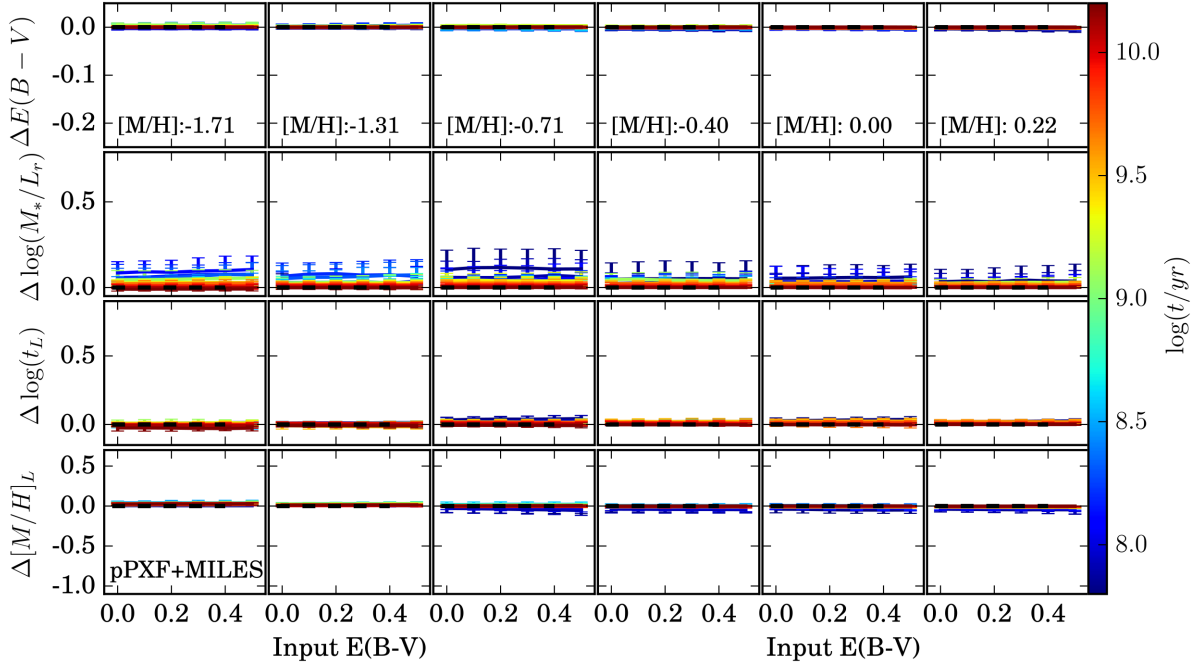


**Figure 10.** The pPXF fitting of mock spectra generated by a single SSP as a function of the stellar age and metallicity at  $S/N = 60$ . Lines in different panels are the same as shown in Fig. 9.

codes by combining two different SSPs with solar metallicity. We take a set of 13 SSPs with solar metallicity, logarithmically spaced in age between 0.063 and 15.8 Gyr (i.e. we skip every other age from our full set of SSPs), and consider all 78 combinations of two SSPs without repetition. The two selected SSPs are co-added together after normalizing fluxes to 1 at  $\lambda = [5490, 5510] \text{ \AA}$ . Then

we perform the simulation with the same steps as the single SSP tests.

The age and metallicity of two-component SSPs co-added spectra, which can have light-weighted values defined in equations (2–8) and mass-weighted values defined as follows:

$$\log t_M = \sum f_{M,i} \times \log t_i, \quad (9)$$

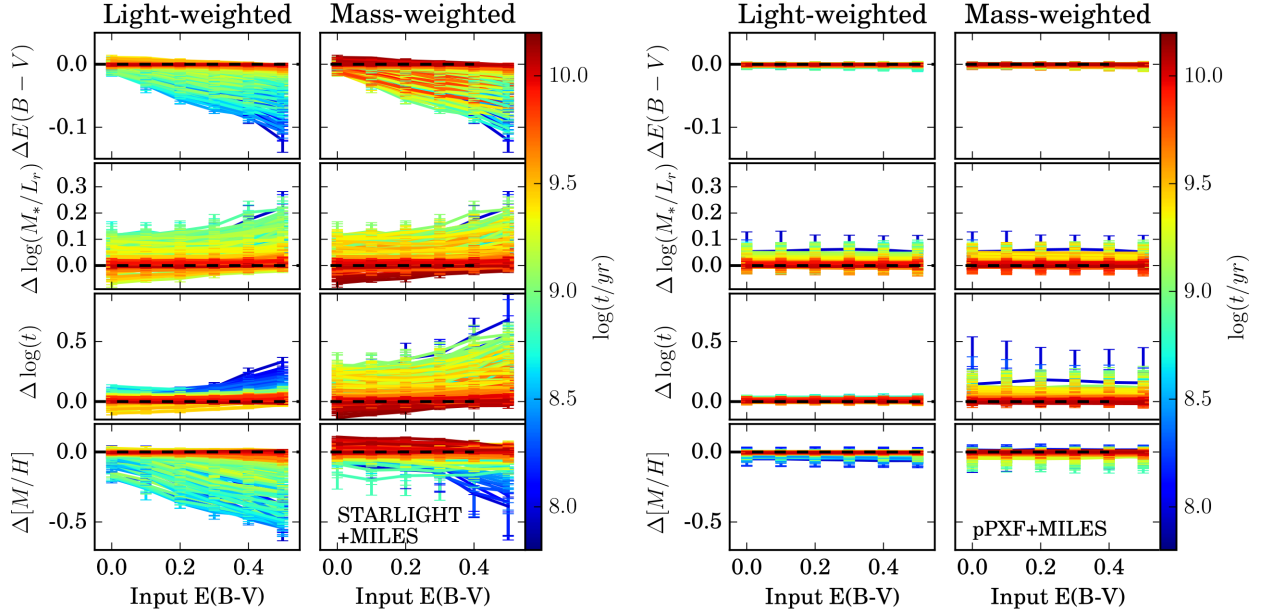


**Figure 11.** Full-spectrum fitting results of two-component SSPs co-added mock spectra at solar metallicity with  $S/N = 60$ . The first and second columns show the light-weighted and mass-weighted results by STARLIGHT, while the third and fourth columns show the corresponding results by pPXF. Colours in the first and third columns represent the light-weighted ages, while those colours in the second and fourth columns correspond to mass-weighted ages. For  $E(B - V)$  and  $M*/L_r$  (the first and second rows), the curves are identical between light-weighted and mass-weighted cases, although they are coloured differently by the input ages. The zero-biased line of each parameter is labelled with a horizontal dashed line.

$$[M/H]_M = \sum f_{M,i} \times [M/H]_i. \quad (10)$$

we then calculate the biases of age and metallicity, respectively, as follows:

$$\Delta \log t_M = \frac{1}{N} \sum_i \log t_{M,i} - \log t_{M,\text{input}}, \quad (11)$$

$$\Delta [M/H]_M = \frac{1}{N} \sum_i [M/H]_{M,i} - [M/H]_{M,\text{input}}. \quad (12)$$

We also select the 16th and 84th percentiles of the measured parameter distribution from 50 simulations as  $1\sigma$  error bars.

Fig. 11 shows the fitting results of two-component SSPs co-added mock spectra obtained from STARLIGHT (left two columns) and pPXF (right two columns), respectively. For STARLIGHT, the light-weighted parameter biases and scatters increase at  $E(B - V) > 0.3$  for those spectra with  $\log(t_L/\text{yr}) < 9.5$ . More spectra with middle ages ( $8.5 < \log(t_L/\text{yr}) < 9.5$ ) have increased parameter biases ( $> 1\sigma$ ) compared to single-SSP case (Fig. 9). For pPXF, the light-weighted results are consistent with those in the single-SSP case (Fig. 10).

During the spectral fitting, a significant fraction of mass in an old population can be hidden if it produces little light. Therefore, the light-weighted population parameters, which are more directly linked to the light coming from the spectra, are always more accurate than mass-weighted ones. This is clearly shown in the third row of Fig. 11 for both pPXF and STARLIGHT, where the measured light-weighted stellar ages have smaller biases and scatters than mass-weighted ones. While for the measured  $[M/H]$ , the contaminating old SSPs with significant mass fractions but small light fractions can have both lower and higher  $[M/H]$  (see the examples shown in Fig. 5), hence the mass-weighted  $[M/H]$  has only larger scatters but no obvious larger biases than light-weighted ones.

From the tests based on co-added mock spectra of two-component SSPs, which mimics the observed galaxy spectra better than a single

SSP, we can see that pPXF recovers the input parameters well for all input  $E(B - V)$  cases. While for STARLIGHT, those young spectra with  $t < 3$  Gyr tend to have larger biases with younger stellar ages. For those spectra older than 3 Gyr, although biases still exist, their fitting results become closer to the true values.

## 4 DISCUSSION

According to our analyses, the full-spectrum fitting results from STARLIGHT and pPXF show quite different parameter dependences and bias trends. The pPXF code, which performs the fitting optimization as a quadratic problem, can always converge to the best solution in a finite number of steps. The STARLIGHT code, which is based on Monte Carlo Markov Chains and annealing loops, has significant dependences on many parameters, such as fitting weights of different absorption lines, clipping, number of Markov Chains, and loops.

### 4.1 STARLIGHT fitting improvement by changing line weights and clipping

In STARLIGHT, one can mask emission lines by setting their weights to zero in the ‘Masks.EmLines.SDSS.gm’ file, and can also give more weights to absorption lines (e.g.  $10\times$  or  $20\times$  weights to Ca II K and G-band) to improve the fit. As shown in Fig. 2, the dust extinction correction becomes worse for larger input  $E(B - V)$ . In the case of  $\log(t/\text{yr}) = 8$  with input  $E(B - V) = 0.5$  (left column), the fitted  $E(B - V)$  is underestimated by 0.2 mag, which corresponds to  $\Delta E(B - V) = -0.2$ . If one gives 10 times more weight to the Ca II K and G-band,  $\Delta E(B - V)$  is reduced to  $-0.1$  mag.

As shown in the bottom right panel of Fig. 5, there are many SSP components with very small light fractions but relatively large mass fractions, which are mainly due to the flux uncertainty that makes the light scattered to larger ages. These components cannot be taken

seriously due to their small light fractions (e.g. those black boxes with light fraction  $< 1$  per cent). However, the parameter biases are mainly caused by those SSP components with large light/mass fractions (e.g.  $> 10$  per cent). In the latest published STARLIGHT code,  $A_V < 1$  is imposed when initializing the Markov Chains (Roberto Cid Fernandes, private communication), which actually constrains the search of the minimum  $\chi^2$  when the true  $A_V$  is larger than 1 mag. Based on the current initialization set-up, fitting spectra with  $A_V < 1$  can converge more easily than those spectra with  $A_V > 1$ . This prior explains why the spectra with input  $E(B - V) \leq 0.2$  show better convergence results than those with input  $E(B - V) > 0.2$ . When fitting spectra with  $A_V > 1$ , increasing the number of Markov Chains and annealing loops is a possible way to improve the fitting quality.

Therefore, we test a ‘slow’ mode (as described at the end of the config file ‘StCv04.C11.config’) set-up of STARLIGHT fitting in the appendix, by increasing the number of chains and loops but keeping other parameters the same as shown in Section 2.3. When applying the ‘slow’ mode parameter set-up, the spectral fitting results show significant improvements.

Based on the above analyses, the STARLIGHT fitting results can be improved by setting different priors, number of Markov Chains, and annealing loops, etc. The current default set-up, which is established already based on lots of efforts, still requires large improvement especially on fitting those spectra with large dust extinctions, e.g.  $E(B - V) > 0.2$ .

## 4.2 Understanding our fitting results

The parameter biases shown in Figs 2 and 3 can be interpreted as due to two effects: (1) For STARLIGHT with input  $E(B - V) > 0.2$ , the results are mainly biased by the small starting value in  $E(B - V)$  in the current version of the code, which produces slow convergence of the chain for large  $E(B - V)$ . This could be easily fixed in the code (Cid Fernandes, private communication). (2) Apart from this issue, both PPXF and STARLIGHT have similar trends with S/N. The main bias is caused by the well-known outshining effect: when the spectrum light is completely dominated by a young population, at low S/N it becomes possible to ‘hide’ significant mass fractions from old populations, due to their relatively large  $M_*/L$ . This effect explains (1) why younger spectra have stronger parameter biases, and (2) why the biases in age and  $M_*/L_r$  are always positive. Negative biases in  $[M/H]_L$  are then induced, which can be explained by the age-metallicity degeneracy, to keep the fit unchanged. At low S/N, the noise washes away the differences between spectrally similar templates, which enlarge the measured parameter scatters.

The volume limitation in both age and metallicity grids is a possible reason for introducing parameter biases, especially when the input value is near the edge of the model grid. If the age grid limitation dominates the age bias, then we can derive positive age bias at  $\log(t/\text{yr}) = 8.0$  case, and negative bias at  $\log(t/\text{yr}) = 10.0$  case. However, we do not see this trend. The parameter biases for  $\log(t/\text{yr}) = 8.0$  (at the edge of age grid) and  $\log(t/\text{yr}) = 9.5$  (in the middle of age grid) show similar trends (see the third column of Fig. 4). The selected solar metallicity is close to the edge of metallicity grid. To check whether the results are limited by model grids, we do the same test as shown in Figs 2 and 3 for ages  $\log(t/\text{yr}) = 8.0, 8.5, 9.0, 9.5, 10.0$  at  $[M/H] = -0.4$ , at the middle of the metallicity grid. The derived results are very similar to that shown in Figs 2 and 3, which suggest that the current biases are not caused by the limitation of metallicity grid. Here, we do not show the  $[M/H] = -0.4$  related results as new figures because of their high similarity to Figs 2 and 3.

## 4.3 Execution time comparisons

When applying the PPXF (in PYTHON) and STARLIGHT (in Fortran) codes for spectral fitting, their computation times vary greatly. The fitting times are affected by many parameters, such as the spectral S/N and different fitting set-ups (e.g. number of Markov Chains and annealing loops for STARLIGHT fitting). For example, for the settings described above, for Mac Os X10.8, PYTHON version 2.7.2 and GCC version 4.8.1, the PPXF code can fit a spectrum with  $\log(t/\text{yr}) = 9$ ,  $[M/H] = 0$ , input  $E(B - V) = 0.2$ , S/N = 60 and a flat-shape error spectrum, in  $\sim 0.8$  s, while STARLIGHT takes  $\sim 56$  s, which means PPXF is 70 times faster than STARLIGHT.

The STARLIGHT fitting with the ‘slow’ mode takes more time to run. Compared to the default set-up, the ‘slow’ mode fitting is 11 times slower than the default set-up, and 770 times slower than PPXF fitting.

Note that both PPXF and STARLIGHT are fitting in the limit of a large number (150 in this work) of parameters, namely the weights of the SSPs. The PPXF solves for these (linear) parameters using an efficient quadratic programming algorithm, while STARLIGHT solves these as general non-linear parameters. This implies that to speed up STARLIGHT significantly would require a major algorithmic change.

## 4.4 Parameter biases at S/N = 30

For the current galaxy IFU surveys, spaxels around a galaxy’s edge usually have S/N  $< 10$  (typically  $\sim 1$ ), which means that spatial rebinning is required to improve the corresponding S/N before the spectral fitting analysis. Limited by spatial resolution and S/N of each spaxel, S/N = 30 is an optional value (e.g. Li et al. 2017) selected for Voronoi 2D binning (Cappellari & Copin 2003), which provides a higher S/N for spectral fitting and better spatial resolution for scientific analyses.

For STARLIGHT with the default set-up, results obtained from S/N = 30 (Fig. B1) have the same level of biases and scatters as the S/N = 60 case (Fig. 2), which means these results are strongly biased for those spectra with large dust extinction (e.g.  $E(B - V) \geq 0.3$ ) and young ages (e.g.  $t < 10^9$  yr). For PPXF at S/N = 30 (Fig. B2), the dust extinction can be recovered well as the S/N = 60 case (Fig. 10). Given a spectrum with  $t = 10^8$  yr and solar metallicity at S/N = 30, which is close to the worst-fitting results of PPXF, the parameter bias is 0.06 dex in  $M_*/L_r$ , 0.03 dex in both age and  $[M/H]$  (see also Fig. 4).

## 5 CONCLUSION

In this paper, we have examined the performance of two full-spectrum fitting algorithms (STARLIGHT and PPXF) in deriving basic stellar population parameters. We run the most basic input–output test in the absence of model uncertainties and with simple SFH including only one or two SSPs. We use SSPs included in Vazdekis/MILES stellar population library to generate mock spectra, and also use this library to do the spectral fitting. We use the same extinction curve in generating and fitting spectra. This avoids model biases due to incorrect IMF, dust reddening curve, stellar evolution model, and empirical stellar spectral library, thus giving us a chance to purely study the effect of observational errors and algorithm biases on the fitting results. We do this to set a baseline for the minimum errors one would have with these full-spectrum fitting methods.

Even for such basic tests, as soon as we add noise and extinction, the algorithms could introduce systematic bias to the fitted parameters. In most cases, PPXF produces better accuracy on the derived



parameters than STARLIGHT, and is 2–3 orders of magnitude faster to run.

In particular, for young and intermediate age population with significant dust extinction, STARLIGHT yields significant biases in the resulting parameters. This is likely due to the slow convergence of the Markov Chain and annealing loops. Adopting the ‘slow’ mode set-up (see appendix) with a larger number of Markov Chains and annealing loops reduces the bias somewhat but is still not as good as PPXF. STARLIGHT fitting results also show a clear dependence on the shape of the error spectrum.

The accuracy of the derived parameters by PPXF are nearly independent of the shape of the error spectrum and the level of dust extinction. Unlike STARLIGHT, the accuracy of parameters improves quickly with increasing S/N of the spectra, as expected. The systematic bias and uncertainty of the fitted parameters also depend sensitively on the intrinsic age of the stellar population. Spectra of younger populations always result in larger bias and scatter (in logarithmic space) than older stellar populations.

We encourage users of other full-spectrum fitting methods to also conduct such basic input–output tests to understand the inherent bias and scatter imposed by the observational errors and the algorithm of choice. These sets the floor of uncertainties one can expect. They can also be used to motivate the choice of S/N thresholds one wants to adopt in observations and reduction of the data.

## ACKNOWLEDGEMENTS

We would like to thank to the anonymous referee for the suggestions that helped to improve this paper. We thank R. Cid Fernandes for his useful comments on our STARLIGHT fitting results, and A. L. de Amorim for providing us their STARLIGHT fitting set-up. This work is supported by the National Natural Science Foundation of China (NSFC) under grant number 11473032 (JG), 11333003 (SM), 11390372 (SM, YL), and 11690024 (YL). RY acknowledges support by National Science Foundation grant AST-1715898. MC acknowledges support from a Royal Society University Research Fellowship.

## REFERENCES

Albareti F. D. et al., 2017, *ApJS*, 233, 25  
 Arimoto N., Yoshii Y., 1987, *A&A*, 173, 23  
 Bertelli G., Bressan A., Chiosi C., Fagotto F., Nasi E., 1994, *A&AS*, 106, 275  
 Bica E., 1988, *A&A*, 195, 76  
 Bressan A., Chiosi C., Fagotto F., 1994, *ApJS*, 94, 63  
 Bruzual G., 1983, *ApJ*, 273, 105  
 Bruzual G., Charlot S., 1993, *ApJ*, 405, 538  
 Bruzual G., Charlot S., 2003, *MNRAS*, 344, 1000  
 Bundy K. et al., 2015, *ApJ*, 798, 7  
 Buzzoni A., 1989, *ApJS*, 71, 817  
 Calzetti D., Armus L., Bohlin R. C., Kinney A. L., Koornneef J., Storchi-Bergmann T., 2000, *ApJ*, 533, 682  
 Cappellari M., 2017, *MNRAS*, 466, 798  
 Cappellari M., Copin Y., 2003, *MNRAS*, 342, 345  
 Cappellari M., Emsellem E., 2004, *PASP*, 116, 138  
 Cappellari M. et al., 2012, *Nature*, 484, 485  
 Charlot S., Bruzual A. G., 1991, *ApJ*, 367, 126  
 Chen Y., Trager S., Peletier R., Lancon A., 2011, *J. Phys.: Conf. Ser.*, 328, 012023  
 Cid Fernandes R., Sodre L., Schmitt H. R., Leao J. R. S., 2001, *MNRAS*, 325, 60  
 Cid Fernandes R., Mateus A., Sodre L., Stasinska G., Gomes J. M., 2005, *MNRAS*, 358, 363

Conroy C., 2013, *ARA&A*, 51, 393  
 Conroy C., Gunn J. E., White M., 2009, *ApJ*, 699, 486  
 Cordier D., Pietrinferni A., Cassisi S., Salaris M., 2007, *AJ*, 133, 468  
 de Amorim A. L. et al., 2017, *MNRAS*, 471, 3727  
 Faber S. M., 1972, *A&A*, 20, 361  
 Fioc M., Rocca-Volmerange B., 1997, *A&A*, 326, 950  
 Gallazzi A., Bell E. F., 2009, *ApJS*, 185, 253  
 Girardi L., Bressan A., Bertelli G., Chiosi C., 2000, *A&AS* 141, 371  
 Gomes J. M., Papaderos P., 2017, *A&A*, 603, A63  
 Graves G. J., Faber S. M., 2010, *ApJ*, 717, 803  
 Gregg M. D. et al. 2006, In Koekemoer A. M., Goudfrooij P., Dressel L. L., eds, *The 2005 HST Calibration Workshop: Hubble After the Transition to Two-Gyro Mode: Proceedings of a Workshop Held at the Space Telescope Science Institute, Baltimore, Maryland. NASA, USA*  
 Guiderdoni B., Rocca-Volmerange B., 1987, *A&A*, 186, 1  
 Gunn J. E., Stryker L. L., 1983, *ApJS*, 52, 121  
 Heap S. R., Lindler D., 2011, in Johns-Krull C., Browning M. K., West A. A., eds, *ASP Conf. Ser. Vol. 448, Atmospheric Parameters of Stars in Hubble’s Next Generation Spectral Library*, Astron. Soc. Pac., San Francisco, 887  
 Jones B. J. T., 1999, *MNRAS*, 307, 376  
 Kauffmann G. et al., 2003, *MNRAS*, 341, 33  
 Koleva M., Prugniel Ph., Bouchard A., Wu Y., 2009, *A&A*, 501, 1269  
 Lawson C. L., Hanson R. J., 1995, *Solving Least Squares Problems. Classics in Applied Mathematics*, Vol. 15. SIAM, PA, USA  
 Le Borgne J. F. et al., 2003, *A&A*, 402, 433  
 Lee S. K., Idzi R., Ferguson H. C., Somerville R. S., Wiklund T., Gialalisco M., 2009, *ApJS*, 184, 100  
 Leitherer C., Heckman T. M., 1995, *ApJS*, 96, 9  
 Leitherer C. et al., 1999, *ApJS*, 123, 3  
 Li H. Y., Ge J. Q., Mao S., Cappellari M., 2017, *ApJ*, 838, 77  
 Maraston C., 1998, *MNRAS*, 300, 872  
 Maraston C., Stromback G., 2011, *MNRAS*, 418, 2785  
 Marigo P., Girardi L., Bressan A., Groenewegen M. A. T., Silva L., Granato G. L., 2008, *A&A*, 482, 883  
 Martino L., Del Olmo V. P., Read J., 2012, *Stat. Probab. Lett.*, 82, 1445  
 McClure R. D., van den Bergh S., 1968, *AJ*, 73, 313  
 McDermid R. M. et al., 2015, *MNRAS*, 448, 348  
 Meynet G., Maeder A., 2000, *A&A*, 361, 101  
 Morelli L., Calvi V., Masetti N., Parisi P., Landi R., Maiorano E., Minniti D., Galaz G., 2013, *A&A*, 556, A135  
 Morelli L., Corsini E. M., Pizzella A., Dalla Bontà E., Coccato L., Méndez-Abreu J., 2015, *MNRAS*, 452, 1128  
 Mouldaka J., Boisson C., Joly M., Pelat D., 2004, *A&A*, 420, 459  
 Muzzin A., Marchesini D., van Dokkum P. G., Labbe I., Kriek M., Franx M., 2009, *ApJ*, 701, 1839  
 Ocvirk P., Pichon C., Lançon A., Thiébaud E., 2006, *MNRAS*, 365, 46  
 Onodera M. et al., 2012, *ApJ*, 755, 26  
 Papovich C., Dickinson M., Ferguson H. C., 2001, *ApJ*, 559, 620  
 Pelat D., 1997, *MNRAS*, 284, 365  
 Pforr J., Maraston C., Tonini C., 2012, *MNRAS*, 422, 3285  
 Pickles A. J., 1998, *PASP*, 110, 863  
 Pietrinferni A., Cassisi S., Salaris M., Castelli F., 2004, *ApJ*, 612, 168  
 Prugniel P., Soubiran C., 2001, *A&A*, 369, 1048  
 Rayner J. T., Cushing M. C., Vacca W. D., 2009, *ApJS*, 185, 289  
 Salpeter E. E., 1955, *ApJ*, 121, 161  
 Sanchez S. F. et al., 2011, *MNRAS*, 410, 3135  
 Sanchez S. F., Kennicutt R. C., Gil de Paz A., et al. 2012, *A&A*, 538:A8  
 Sanchez-Blazquez P., Peletier R. F., Jimenez-Vicente J., Cardiel N., Cenarro A. J. et al., 2006, *MNRAS*, 371, 703  
 Schaller G., Schaerer D., Meynet G., Maeder A., 1992, *A&AS*, 96, 269  
 Schulz J., Fritze-v. Alvensleben U., Moller C. S., Fricke K. J., 2002, *A&A*, 392, 1  
 Searle L., Sargent W. L. W., Bagnuolo W. G., 1973, *ApJ*, 179, 427  
 Shapley A. E., Steidel C. C., Adelberger K. L., Dickinson M., Gialalisco M., Pettini M., 2001, *ApJ*, 562, 95  
 Shetty S., Cappellari M., 2015, *MNRAS*, 454, 1332  
 Spinrad H., Taylor B. J., 1971, *ApJS*, 22, 445

- Tinsley B. M., 1968, *ApJ*, 151, 547  
 Tinsley B. M., 1978, *ApJ*, 222, 14  
 Tinsley B. M., Gunn J. E., 1976, *ApJ*, 203, 52  
 Tojeiro R., Heavens A. F., Jimenez R., Panter B., 2007, *MNRAS*, 381, 1252  
 Trager S. C., Faber S. M., Dressler A., 2008, *MNRAS*, 386, 715  
 Valdes F., Gupta R., Rose J. A., Singh H. P., Bell D. J., 2004, *ApJS*, 152, 251  
 Vazdekis A., 1999, *ApJ*, 513, 224  
 Vazdekis A., Sánchez-Blázquez P., Falcón-Barroso J., Cenarro A. J., Beasley M. A., Cardiel N., Gorgas J., Peletier R. F., 2010, *MNRAS*, 404, 1639  
 Walcher J., Groves B., Budavari T., Dale D., 2011, *Astrophys. Space Sci.*, 331, 1  
 Wilkinson D. M. et al., 2015, *MNRAS*, 449, 328  
 Wood D. B., 1966, *ApJ*, 145, 36  
 Worthey G., 1994, *ApJS*, 95, 107  
 Wuyts S., Franx M., Cox T. J., Hernquist L., Hopkins P. F. et al., 2009, *ApJ*, 696, 348  
 York D. G. et al., 2000, *AJ*, 120, 1579  
 Zibetti S., Charlot S., Rix H. W., 2009, *MNRAS*, 400, 1181

## APPENDIX A: STARLIGHT FITTING RESULTS BASED ON LARGER MARKOV CHAINS AND ANNEALING LOOPS

In this paper, we adopt the default set-up but with normalization window changed as done in de Amorim et al. (2017):  $l_{\text{norm}} = 5635 \text{ \AA}$ ,  $l_{\text{low\_norm}} = 5590 \text{ \AA}$ ,  $l_{\text{upp\_norm}} = 5680 \text{ \AA}$ , and  $A_V$  fitting range to  $[-0.5, 4]$  to allow negative  $A_V$  and large enough parameter space

for fitting as described in Cid Fernandes et al. (2005). There are seven Markov Chains and three annealing loops included. We then increase the number of Chains and loops to see whether the parameter biases and scatters can be reduced.

Here, we show the STARLIGHT fitting results based on the ‘slow’ fitting mode that includes 12 Markov Chains and 10 annealing loops. The default fitting mode is more like the ‘medium’ one, which has seven Markov Chains and five annealing loops. The default set-up can give similar fitting results when input  $E(B - V) \leq 0.2$ , which is also tested by Cid Fernandes et al. (2005). While for spectra with higher dust extinction ( $E(B - V) > 0.2$ ), the default set-up will underestimate  $E(B - V)$  much more (at least two times) than the ‘slow’ mode set-up. With increased spectral S/N, the parameter biases (from the ‘slow’ mode fitting) decrease for all the input  $E(B - V)$  cases (Fig. A1), but this decrease is less significant than that from PPXF (Fig. 3). The effects of error spectral types show clearer trends (Fig. A2), which has already been described in Section 3.2. When applying the ‘slow’ mode parameter set-up, the spectral fitting results show significant improvements and are closer to the input for both single-SSP (Fig. A3) and two-component SSP (Fig. A4) tests.

Since the STARLIGHT fitting depends on the length of chains and loops, convergence may not be reached in the default set-up. Unlike STARLIGHT, which solves for the weights as non-linear parameters, PPXF performs the optimization as a quadratic problem and can quickly converge to the best solution in a small number of steps.

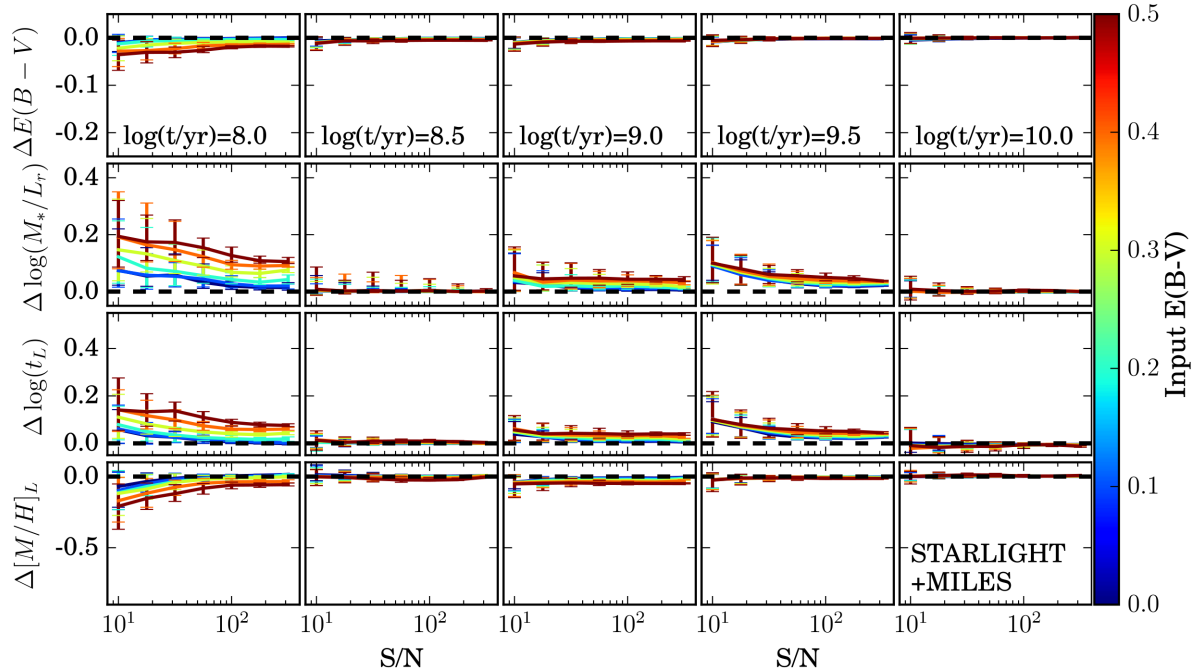


**Figure A1.** The bias and scatter of four stellar population parameters for different spectral S/N’s for STARLIGHT based on the ‘slow’ fitting mode. The lines and colours in each panel are the same as shown in Fig. 2.

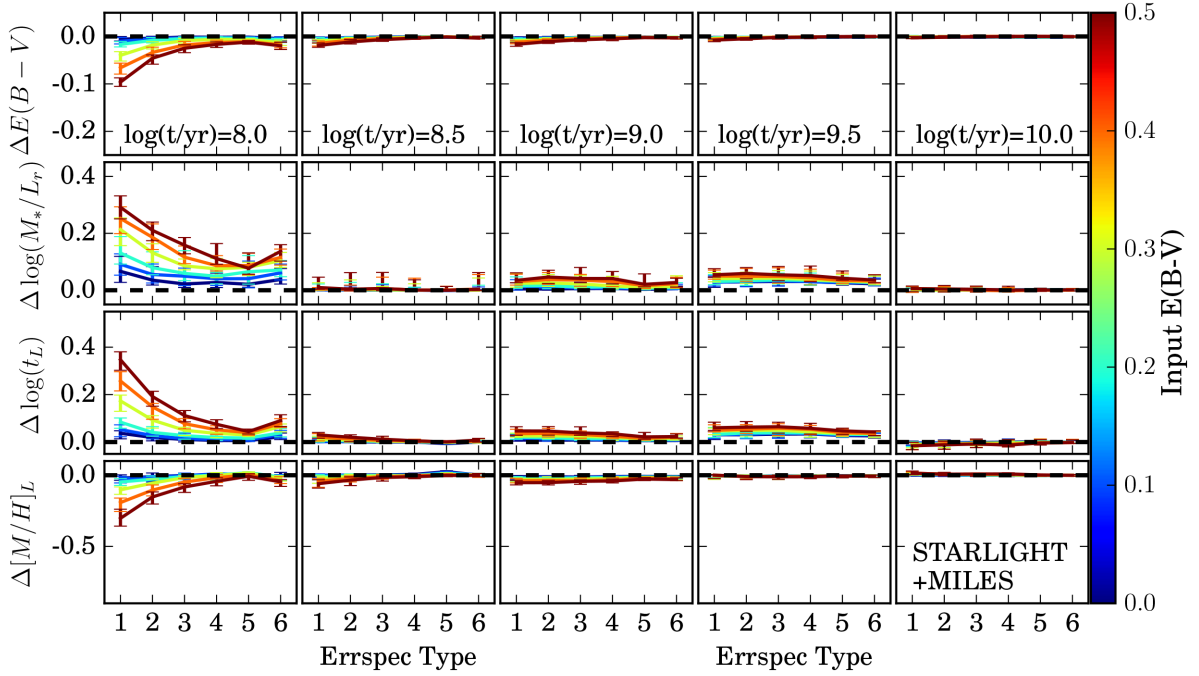


**Figure A2.** STARLIGHT ‘slow’ mode fitting results obtained with six error spectral types at  $S/N = 60$  as shown in Fig. 6. Errspec Type 1–6 corresponding to ET1–ET6. The input  $E(B - V)$  and SSP age set-up are the same as shown in the  $S/N$  test section (Figs 2 and 3).

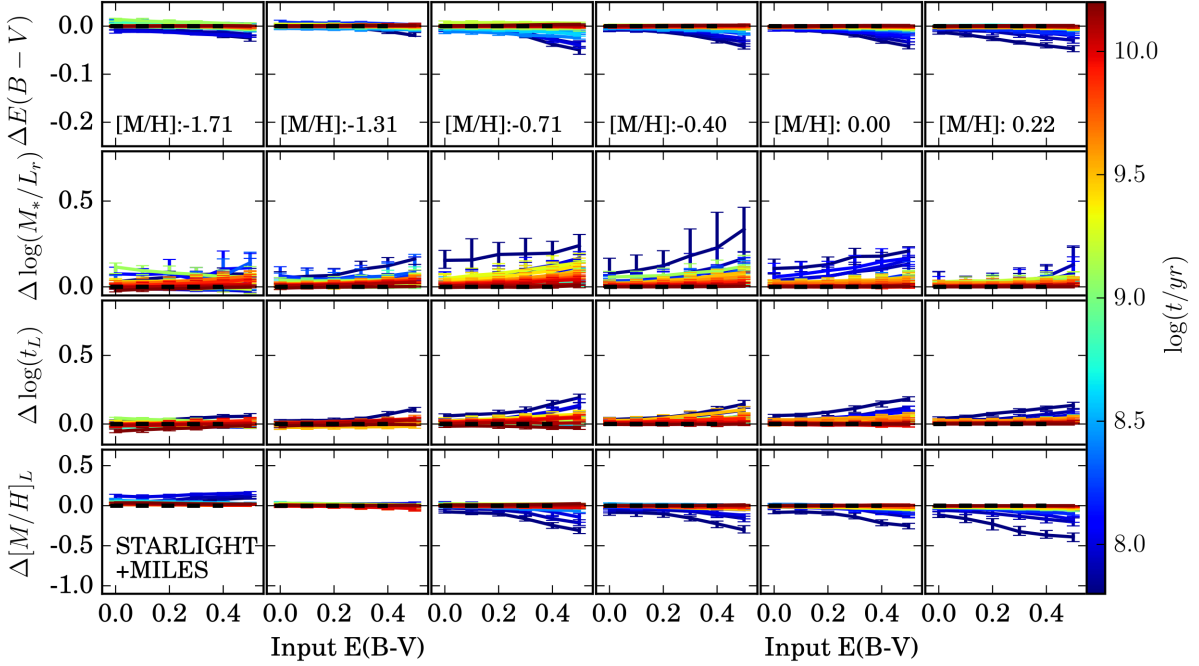


**Figure A3.** STARLIGHT ‘slow’ mode fitting of mock spectra generated by single SSP as a function of the stellar age and metallicity with  $S/N = 60$ . Lines and colours are the same as shown in Fig. 9.

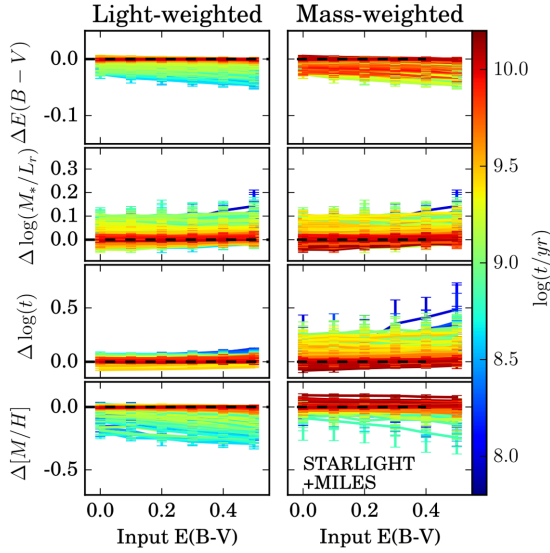


**Figure A4.** STARLIGHT ‘slow’ mode fitting results of two-component mock spectra at solar metallicity with  $S/N = 60$ . Lines and colours are the same as shown in Fig. 11.

## APPENDIX B: THE STARLIGHT AND PPXF FITTING AT $S/N = 30$

The STARLIGHT fitting results with the default set-up at  $S/N = 30$  (Fig. B1) are similar to those at  $S/N = 60$ , which are already shown in Fig. 2.

The PPXF fitting results show increased bias and scatter with decreasing  $S/N$ . Spectral fitting at  $S/N = 30$  can lead to  $\sim 2$  times higher parameter biases and scatters than those at  $S/N = 60$  (Fig. B2).

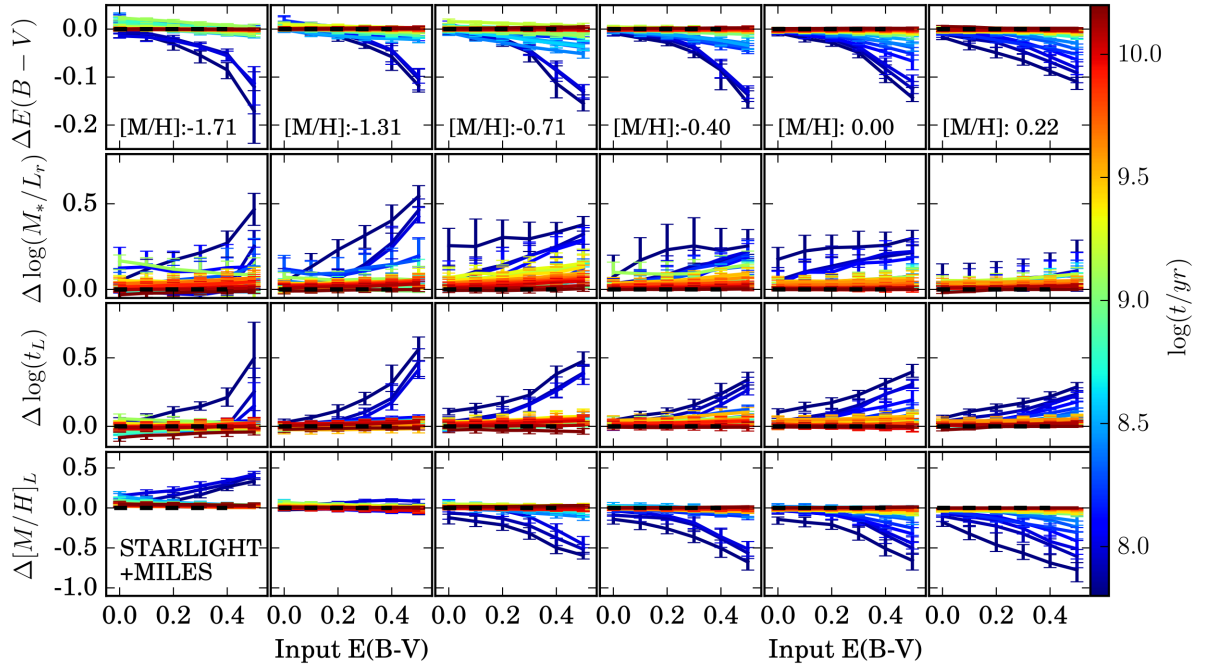


**Figure B1.** The STARLIGHT fitting of mock spectra generated by single SSP varies in the stellar age and metallicity parameter spaces with  $S/N = 30$ . Lines in different panels are the same as shown in Fig. 9.



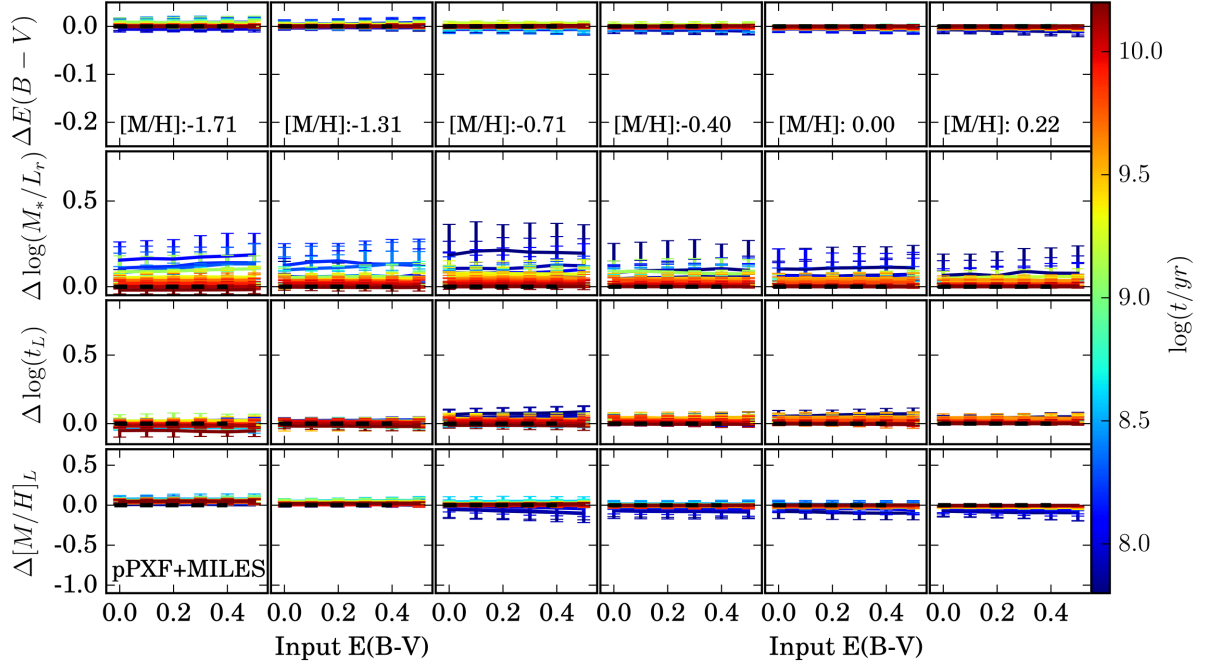


**Figure B2.** The pPXF fitting of mock spectra generated by single SSP varies in the stellar age and metallicity parameter spaces with  $S/N = 30$ . Lines in different panels are the same as shown in Fig. 9.

This paper has been typeset from a  $\text{\LaTeX}$  file prepared by the author.